1746 *J. Phys. Chem. A* **2002,** *106,* 1746−1764

Theoretical Study on Mechanism of the $^3CH_2 + N_2O$ Reaction

Jian-jun Liu, Yi-hong Ding, Ji-kang Feng,* Yu-guo Tao, and Chia-chung Sun

State Key Laboratory of Theoretical and Computational Chemistry, Institute of Theoretical Chemistry, Jilin University, Changchun, Jilin 130023, P. R. China

Received: June 25, 2001; In Final Form: November 29, 2001

The complex triplet potential energy surface of the CH_2N_2O system, including 49 minimum isomers and 114 transition states, is investigated at the B3LYP and QCISD(T) (single-point) levels in order to explore the possible reaction mechanism of the $^3CH_2$ radical with N_2O. The most feasible pathway is the head-on attack of $^3CH_2$ at the terminal N-atom of N_2O to form *cis*-H_2CNNO ($\mathbf{a_1}$) and *trans*-H_2CNNO ($\mathbf{a_2}$). Both $\mathbf{a_1}$ and $\mathbf{a_2}$ can subsequently dissociate to give $\mathbf{P_1}$ (H_2CN + NO) via the direct N−N bond rupture. Much less competitively, $\mathbf{a_1}$ can undergo a 1,4-H shift, leading to the chainlike isomer HCNNOH ($\mathbf{k_1}$), followed by the direct N−N bond cleavage to form product $\mathbf{P_2}$ (HCN + ^{3}HON) or interconversion between the isomers $\mathbf{k_1}$−$\mathbf{k_8}$ and subsequent dissociation to $\mathbf{P_2}$. Furthermore, the products $\mathbf{P_1}$ (H_2CN + NO) and $\mathbf{P_2}$ (HCN + ^{3}HON) can undergo secondary dissociation to the same product $\mathbf{P_{12}}$ (HCN + NO + H). The formation of CO, however, seems impossible due to rather large barriers. Our results are in part contradictory with the recent time-resolved Fourier transform infrared spectroscopic study that nascent vibrationally excited products CO, NO, and HCN were observed. Since the initial N-attack step from **R** to $\mathbf{a_1}$ needs a considerable barrier of 14.8 kcal/mol, the title reaction may only be significant at high temperatures, as confirmed by the ab initio dynamic calculations on the rate constants. The reactivity discrepancies between the triplet and singlet CH_2 with N_2O are compared and discussed in terms of their potential energy surface features. Our calculations suggest that future experimental reinvestigations on the product distributions and rate constants of the title reaction at high temperatures are greatly desired.

1. Introduction

Methylene radical in both singlet and triplet ($^1CH_2$ and $^3CH_2$) is an important intermediate in combustion, atmospheric chemistry, and organic chemistry processes.[1−6] As a highly reactive species, the CH_2 radical can react with nitrous oxide (N_2O), which is known to be a very important intermediate in the conversion in flames from fuel N and atmospheric N_2 to NO.[7] Therefore, the investigation of $CH_2 + N_2O$ reaction plays an important role in decreasing the emitted NO amount.

Experimentally, both $^1CH_2$ and $^3CH_2$ can be produced by laser photolysis of ketene at 308 and 351 nm, respectively.[8] The $^1CH_2 + N_2O$ reaction was found to be very fast around room temperature, with the measured rate constant 6.3×10^{-11} cm^3 molecule^{-1} s^{-1}.[9] Very recently, we calculated the singlet potential energy surface of this reaction,[10] and our results are consistent with the high carbene reactivity of singlet $^1CH_2$. For the $^3CH_2 + N_2O$ reaction, Darwin and Moore[11] studied the reaction kinetics by using time-resolved IR diode laser absorption spectroscopy. They reported an upper bound rate constant of 1.9×10^{-14} cm^3 molecule^{-1} s^{-1} for the overall reaction at 295 K. Simply from the measured rate constants, the reactivity of triplet $^3CH_2$ toward N_2O is expected to be much lower than that of $^1CH_2 + N_2O$, which might be due to their potential energy surface differences. Recently, Su et al.[12] carried out a time-resolved Fourier transform infrared (TR-FTIR) spectroscopy study on the $^3CH_2 + N_2O$ reaction. They observed the nascent vibrationally excited products CO, NO, and HCN (and even possibly N_2H). They also proposed a possible mechanism either via the end-O, N−O π bonding or via N−N π bonding attack. Yet whether such an intuitive mechanism works or not still waits to be tested. It should be pointed out that for the singlet $^1CH_2 + N_2O$ reaction, the most feasible reaction pathways are proceeded via a barrierless end-N attack to form the low-lying intermediate H_2CNNO, followed by direct N−N bond cleavage to form product H_2CN + NO, by a concerted 1,3-H shift and N−N bond rupture to form product HCN + HNO, or by a successive CNNO four-membered ring formation and bimolecular extrusion to give $H_2CO + N_2$. Therefore, a detailed theoretical exploration on the whole triplet potential energy surface of the $^3CH_2 + N_2O$ reaction is still very desirable so as to provide a theoretical interpretation for the $^1CH_2$ and $^3CH_2$ reactivity differences with N_2O.

2. Computational Methods

All calculations are carried out using Gaussian 98 program package.[13] The geometries of all the reactants, products, various intermediates, and transition states for the $^3CH_2 + N_2O$ reaction are optimized using hybrid density functional B3LYP method with the 6-31G(d,p) basis set. Vibrational frequencies are calculated at the B3LYP/6-31G(d,p) level to check whether the obtained stationary point is an isomer or a first-order transition state. To confirm that the transition state connects designated intermediates, we also perform intrinsic reaction coordinate (IRC) calculations at the B3LYP/6-31G(d,p) level. In addition, single-point energies are calculated for the B3LYP/6-31G(d,p) optimized geometries with the quadratic configuration interaction method with single and double excitation as well as perturbative corrections for triple excitations (QCISD(T)) with the 6-311G(d,p) basis set. Unless otherwise specified, the QCISD(T) single-point energies with inclusion of B3LYP/6-31G(d,p) zero-point energies (ZPE) are used in the following discussions.

10.1021/jp0124084 CCC: $22.00

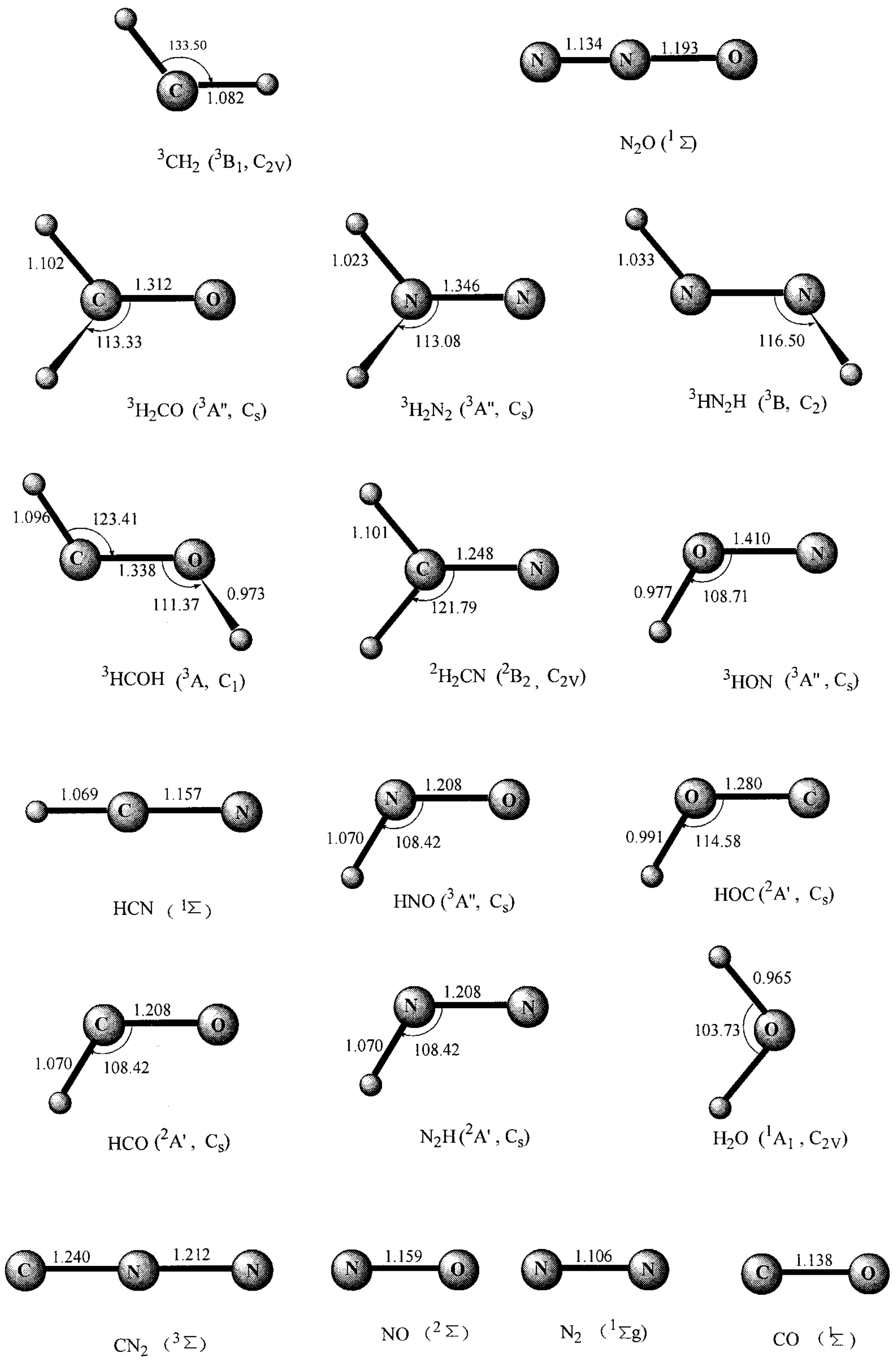

Figure 1. B3LYP/6-31G(d,p)-optimized geometries of reactants and products. Bond distances are in Å, and angles are in deg.

Further, to compare with Darwin and Moore's roughly estimated upper bound rate constant k(295K) for the title reaction,[11] we carry out dynamic calculations using the POLYRATE8.0 program.[14] The theoretical rate constants over the wide temperature range 200−2000 K are calculated using the conventional transition state theory (TST), canonical variational transition state theory (CVT), and canonical variational transition state incorporating small-curvature tunneling correction (CVT/SCT). All internal modes of the transition states, reactants and products are treated as harmonic vibrations.

3. Results and Discussions

For the $^3CH_2 + N_2O$ reaction, various dissociation products, including $\mathbf{P_1}$−$\mathbf{P_{12}}$ (in Figure 1), are considered. A total of 49 intermediate isomers (in Figure 2) and 114 transition states (in Figure 3) are located. The zero-point, total, and relative energies of the products, isomers, and transition states are listed in Tables 1, 2, and 3, respectively. By means of the products, intermediate isomers, transition states, and their corresponding relative energies, the schematic reaction pathways are plotted in Figure

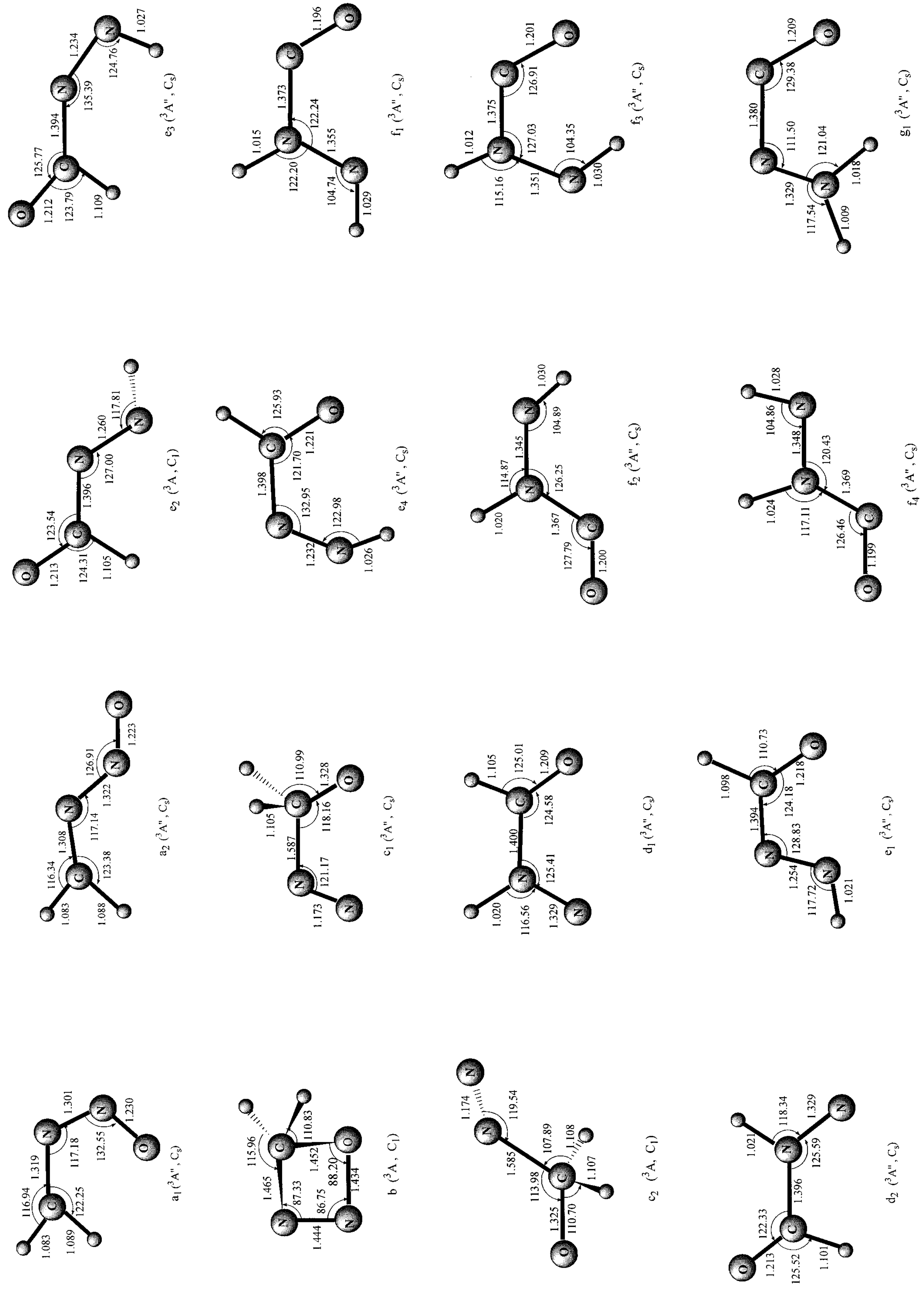

a$_1$ (^{3}A'', C$_s$)

a$_2$ (^{3}A'', C$_s$)

e$_2$ (^{3}A, C$_1$)

e$_3$ (^{3}A'', C$_s$)

b (^{3}A, C$_1$)

c$_1$ (^{3}A'', C$_s$)

e$_4$ (^{3}A'', C$_s$)

f$_1$ (^{3}A'', C$_s$)

c$_2$ (^{3}A, C$_1$)

d$_1$ (^{3}A'', C$_s$)

f$_2$ (^{3}A'', C$_s$)

f$_3$ (^{3}A'', C$_s$)

d$_2$ (^{3}A'', C$_s$)

e$_1$ (^{3}A'', C$_s$)

f$_4$ (^{3}A'', C$_s$)

g$_1$ (^{3}A'', C$_s$)

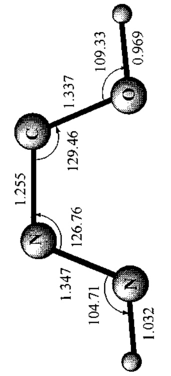

j$_1$ (^{3}A'', C$_s$)

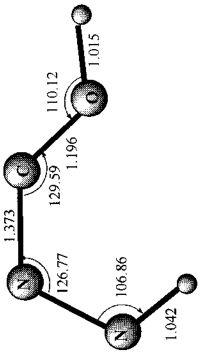

j$_3$ (^{3}A'', C$_s$)

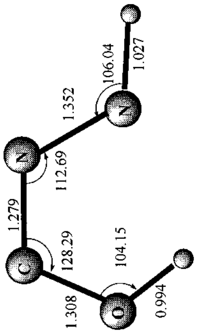

j$_5$ (^{3}A'', C$_s$)

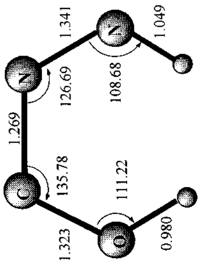

j$_7$ (^{3}A'', C$_s$)

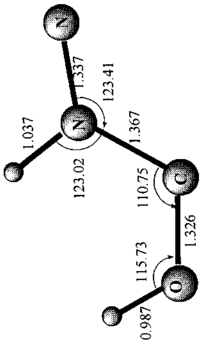

i$_4$ (^{3}A'', C$_s$)

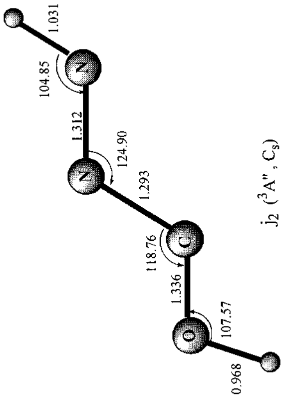

j$_2$ (^{3}A'', C$_s$)

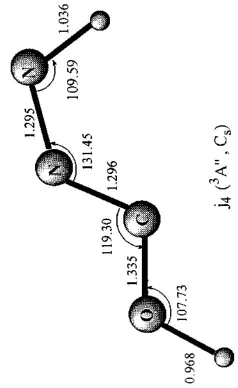

j$_4$ (^{3}A'', C$_s$)

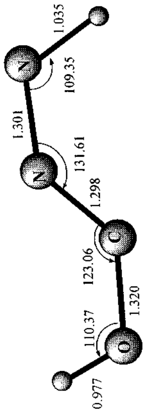

j$_6$ (^{3}A'', C$_s$)

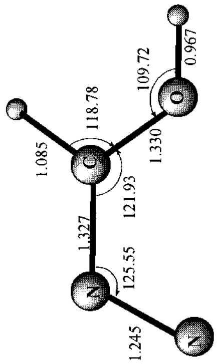

h$_1$ (^{3}A'', C$_s$)

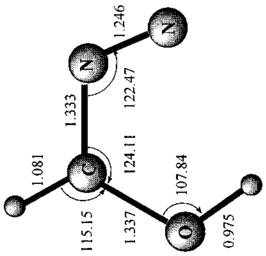

h$_3$ (^{3}A'', C$_s$)

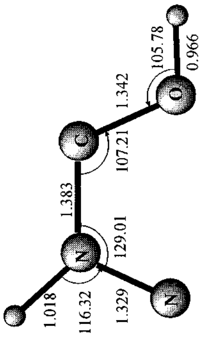

i$_1$ (^{3}A'', C$_s$)

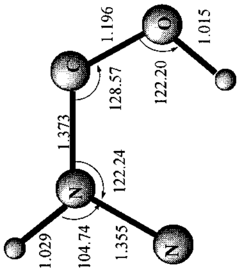

i$_3$ (^{3}A'', C$_s$)

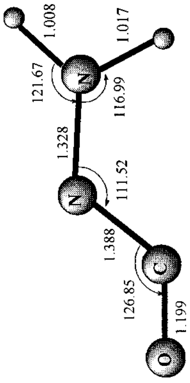

g$_2$ (^{3}A'', C$_s$)

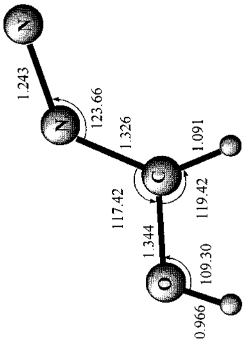

h$_2$ (^{3}A'', C$_s$)

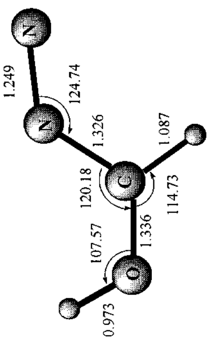

h$_4$ (^{3}A'', C$_s$)

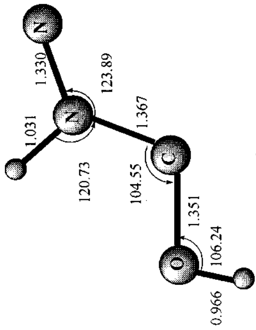

i$_2$ (^{3}A'', C$_s$)

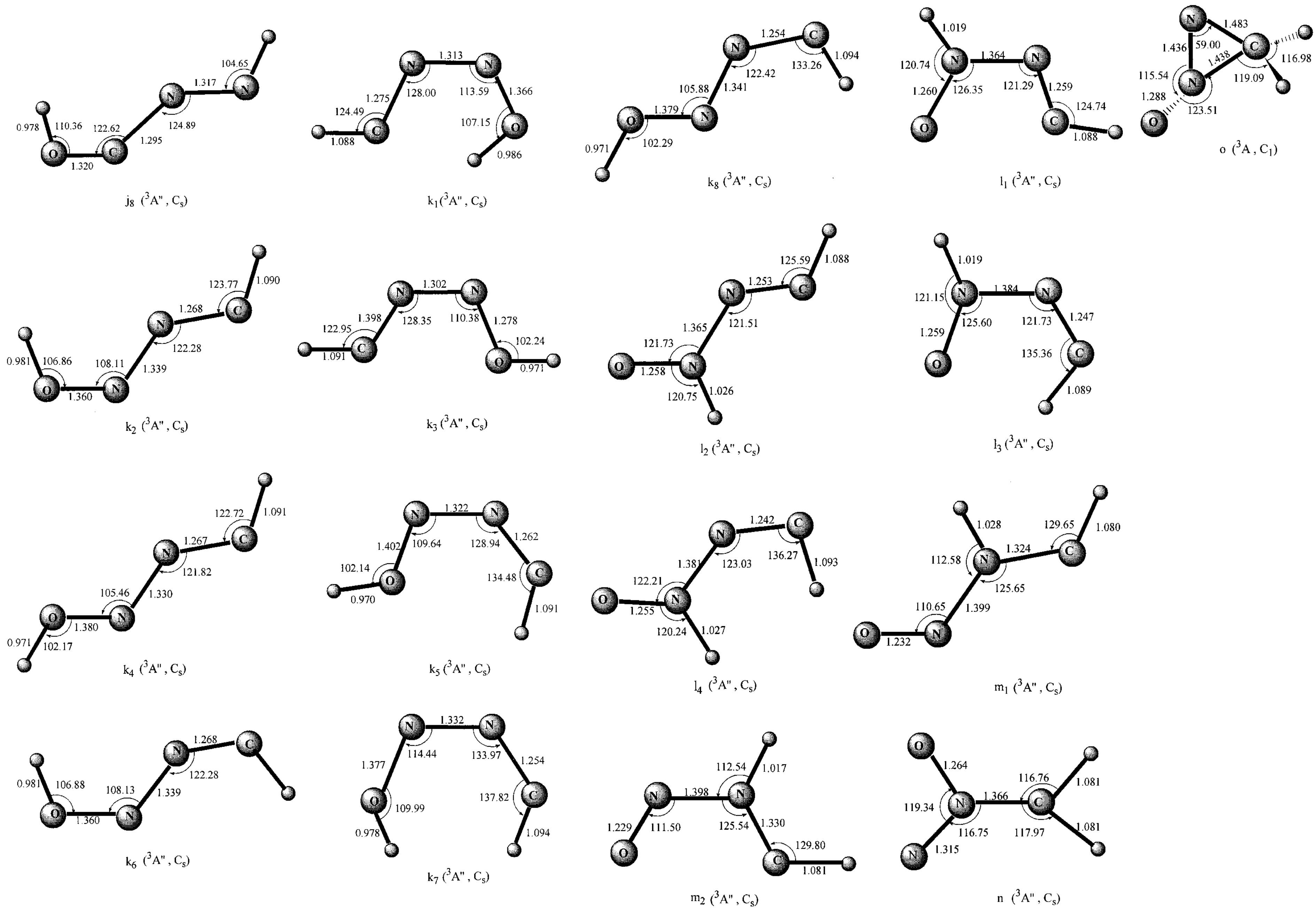

j_8 ($^3A''$, C_s) k_1 ($^3A''$, C_s) k_8 ($^3A''$, C_s) l_1 ($^3A''$, C_s) o (^3A, C_1)

k_2 ($^3A''$, C_s) k_3 ($^3A''$, C_s) l_2 ($^3A''$, C_s) l_3 ($^3A''$, C_s)

k_4 ($^3A''$, C_s) k_5 ($^3A''$, C_s) l_4 ($^3A''$, C_s) m_1 ($^3A''$, C_s)

k_6 ($^3A''$, C_s) k_7 ($^3A''$, C_s) m_2 ($^3A''$, C_s) n ($^3A''$, C_s)

Figure 2. B3LYP/6-31G(d,p)-optimized geometries of all isomers. BBond distances are in Å, and angles are in deg.

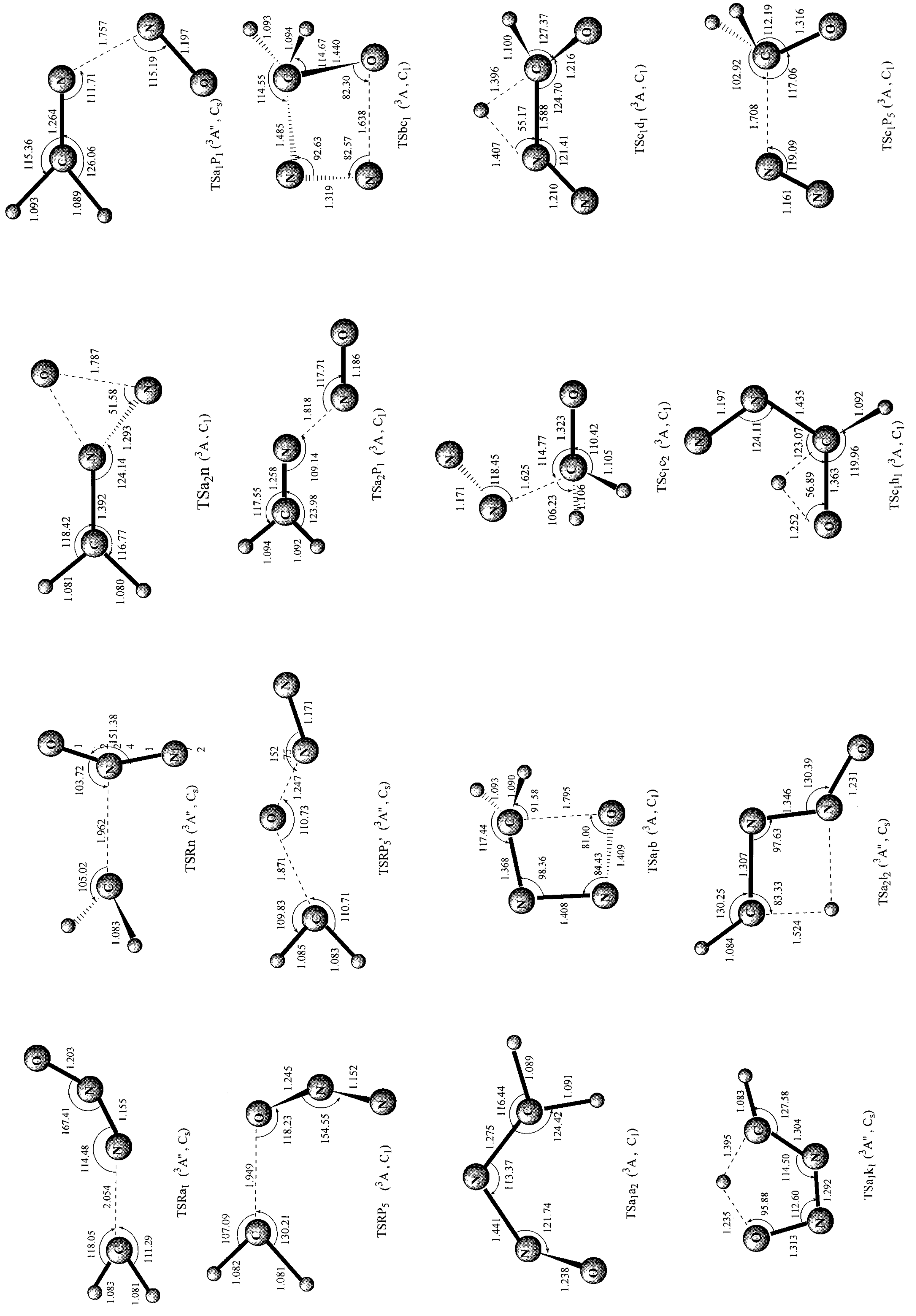

TSc_1P_5 (^3A, C_1)

TSc_1h_1 (^3A, C_1)

TSa_2l_2 ($^3A''$, C_s)

TSa_1k_1 ($^3A''$, C_s)

TSc_1d_1 (^3A, C_1)

TSc_1c_2 (^3A, C_1)

TSa_1b (^3A, C_1)

TSa_1a_2 (^3A, C_1)

$TSbc_1$ (^3A, C_1)

TSa_2P_1 (^3A, C_1)

$TSRP_5'$ ($^3A''$, C_s)

$TSRP_5$ (^3A, C_1)

TSa_1P_1 ($^3A''$, C_s)

TSa_2n (^3A, C_1)

$TSRn$ ($^3A''$, C_s)

$TSRa_1$ ($^3A''$, C_s)

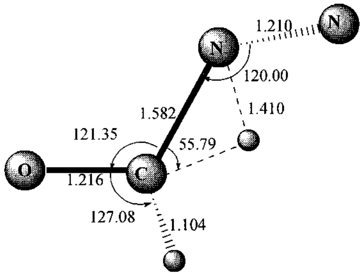

TSc_2d_2 (^3A, C_1)

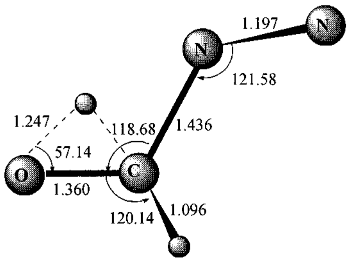

TSc_2h_2 (^3A, C_1)

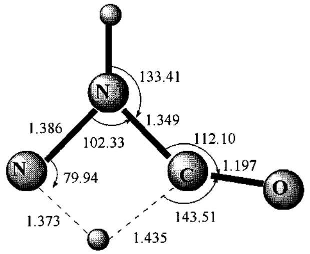

TSd_2f_2 ($^3A''$, C_s)

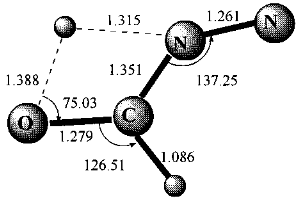

TSd_2h_4 ($^3A''$, C_s)

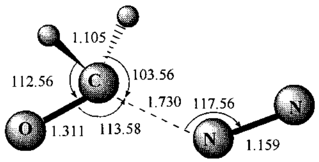

TSc_2P_5 (^3A, C_1)

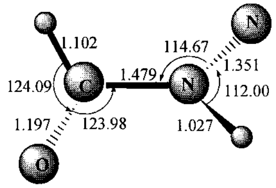

TSd_1d_2 (^3A, C_1)

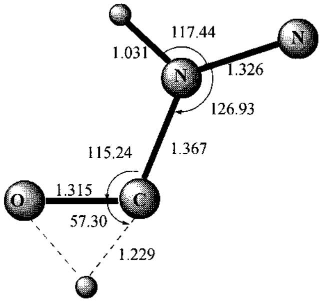

TSd_2i_2 ($^3A''$, C_s)

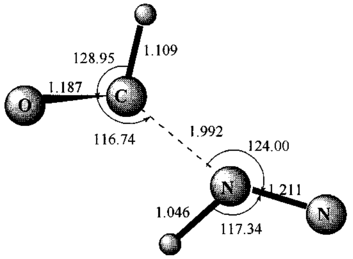

TSd_2P_9 (^3A, C_1)

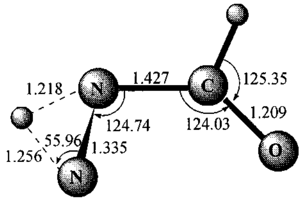

TSd_1e_1 (^3A, C_1)

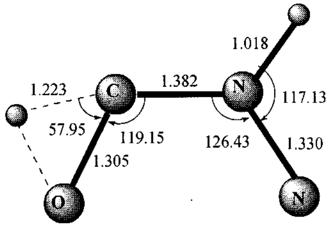

TSd_1i_1($^3A''$, C_s)

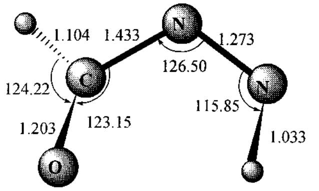

TSe_1e_2 (^3A, C_1)

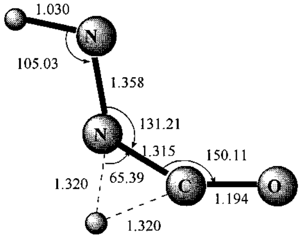

TSe_1f_1 ($^3A''$, C_s)

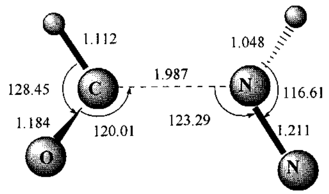

TSd_1P_9 (^3A, C_1)

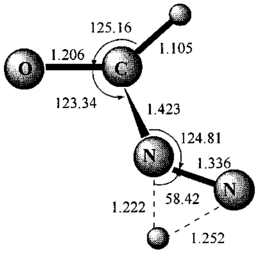

TSd_2e_2 (^3A, C_1)

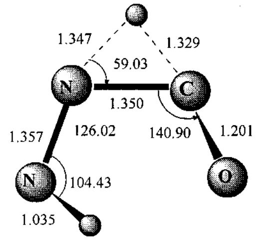

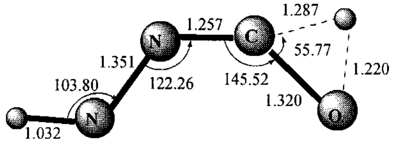

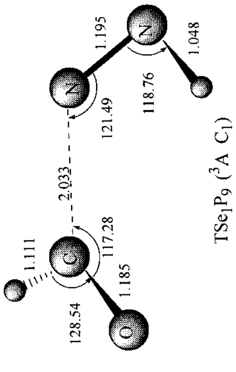

TSe$_1$P$_9$ (^{3}A C$_1$)

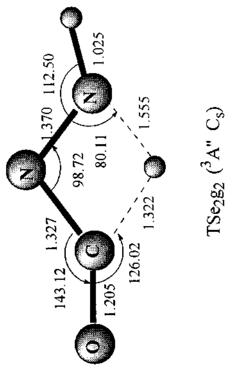

TSe$_2$g$_2$ (^{3}A" C$_s$)

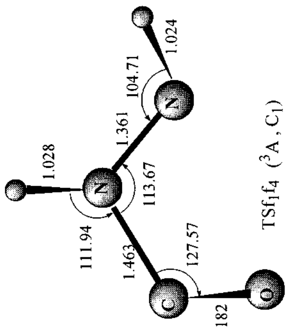

TSf$_1$f$_4$ (^{3}A , C$_1$)

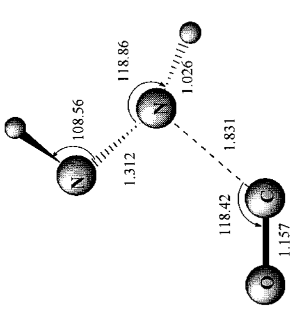

TSf$_1$P$_8$ (^{3}A , C$_1$)

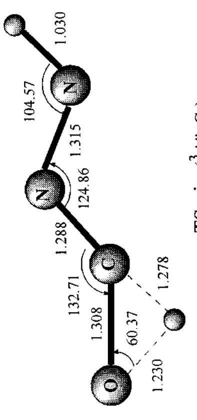

TSe$_2$j$_2$ (^{3}A" C$_s$)

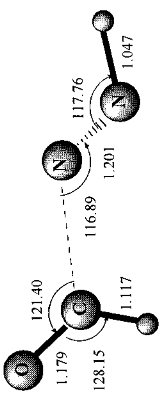

TSe$_2$ P$_9$ (^{3}A C$_1$)

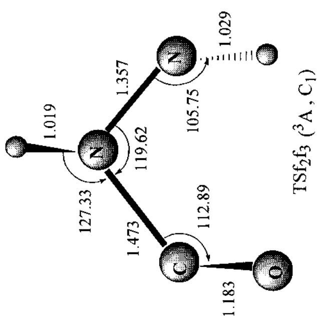

TSf$_2$f$_3$ (^{3}A , C$_1$)

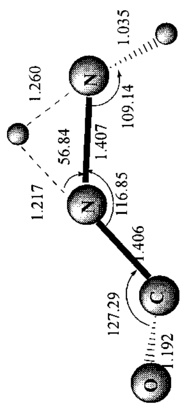

TSf$_2$g$_2$ (^{3}A , C$_1$)

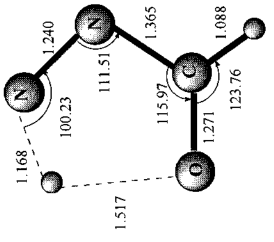

TSe$_3$h$_3$ (^{3}A" C$_s$)

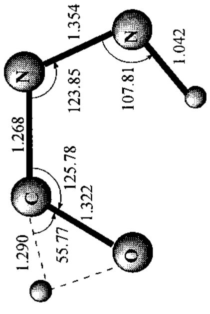

TSe$_3$j$_3$ (^{3}A" C$_s$)

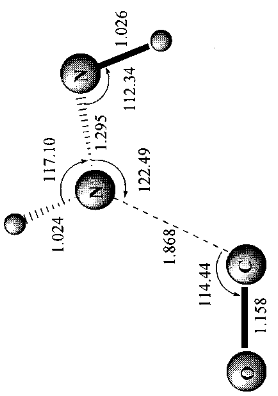

TSf$_2$P$_8$ (^{3}A , C$_1$)

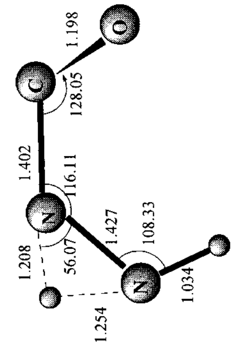

TSf$_3$g$_1$ (^{3}A , C$_1$)

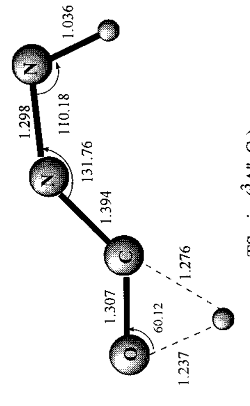

TSe$_4$j$_4$ (^{3}A" C$_s$)

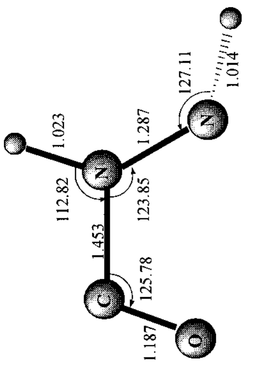

TSf$_1$f$_3$ (^{3}A C$_1$)

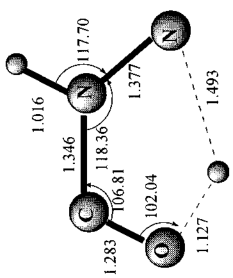

TSf$_3$i$_3$ (^{3}A", C$_s$)

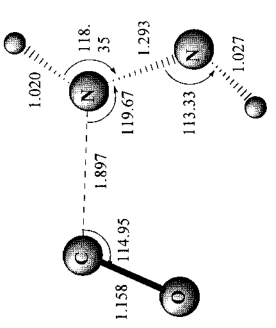

TSf$_3$P$_8$ (^{3}A , C$_1$)

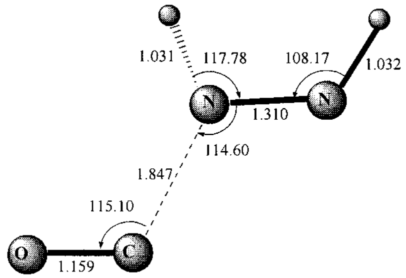

TSf$_4$P$_8$ (^{3}A , C$_1$)

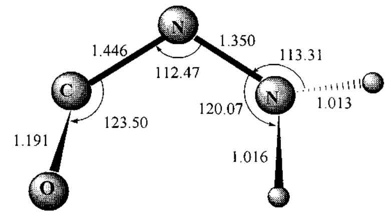

TSg$_1$g$_2$ (^{3}A , C$_1$)

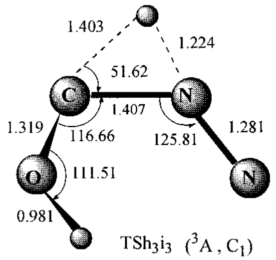

TSh$_3$i$_3$ (^{3}A , C$_1$)

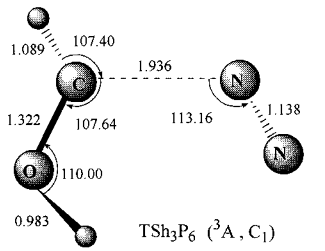

TSh$_3$P$_6$ (^{3}A , C$_1$)

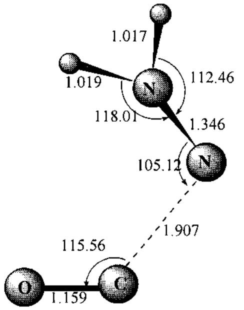

TSg$_1$P$_7$ (^{3}A , C$_1$)

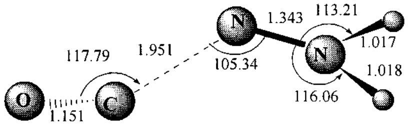

TSg$_2$P$_7$ (^{3}A , C$_1$)

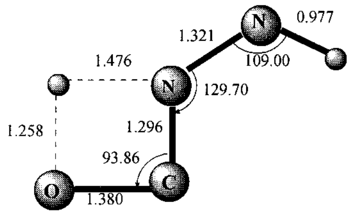

TSh$_4$j$_6$ (^{3}A" , C$_s$)

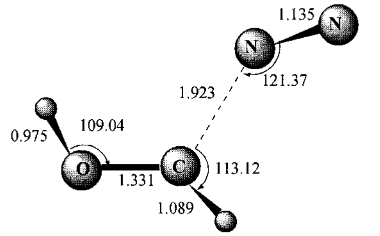

TSh$_4$P$_6$ (^{3}A , C$_1$)

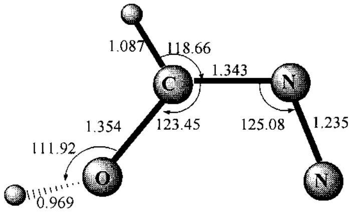

TSh$_1$h$_3$ (^{3}A , C$_1$)

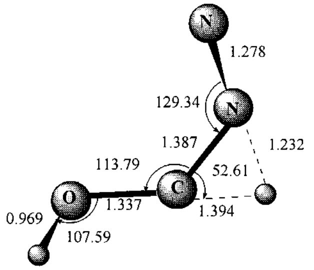

TSh$_1$i$_1$ (^{3}A , C$_1$)

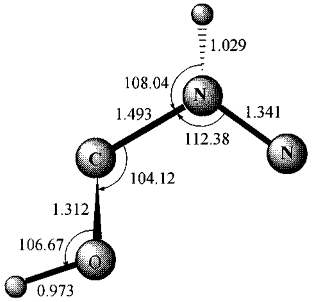

TSi$_1$i$_2$ (^{3}A , C$_1$)

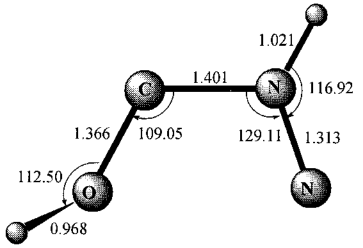

TSi$_1$i$_3$ (^{3}A , C$_1$)

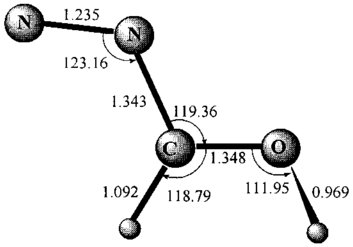

TSh$_2$h$_4$ (^{3}A , C$_1$)

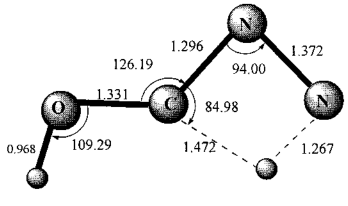

TSh$_2$j$_4$ (^{3}A" , C$_s$)

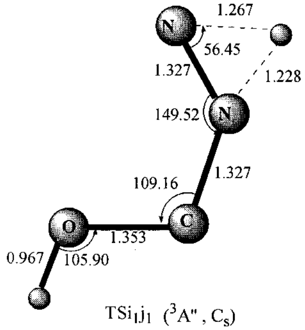

TSi$_1$j$_1$ (^{3}A" , C$_s$)

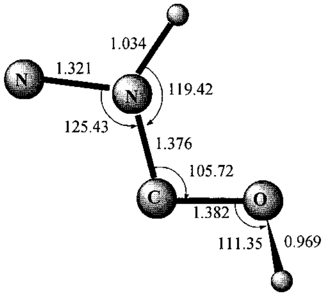

TSi$_2$i$_4$ (^{3}A , C$_1$)

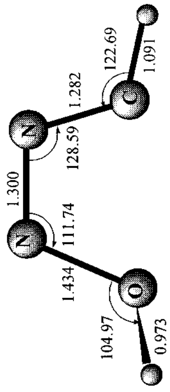

TSk$_1$k$_3$ (^{3}A, C$_1$)

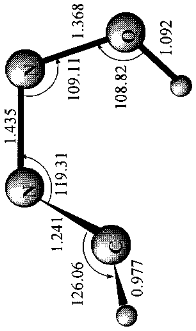

TSk$_1$k$_2$ (^{3}A, C$_1$)

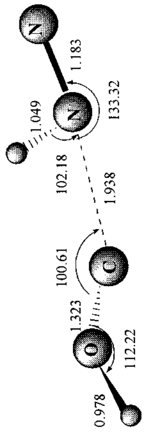

TSi$_2$P$_{10}$ (^{3}A, C$_1$)

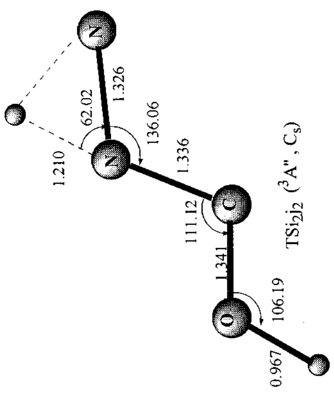

TSi$_2$j$_2$ (^{3}A'', C$_s$)

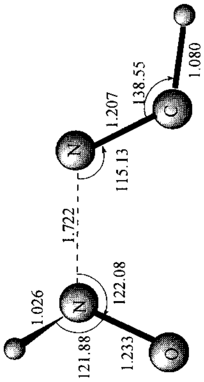

TSk$_1$P$_2$ (^{3}A'', C$_s$)

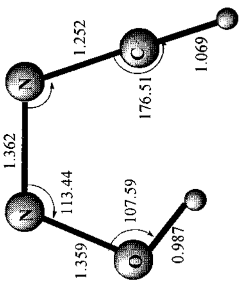

TSk$_1$k$_7$ (^{3}A'', C$_s$)

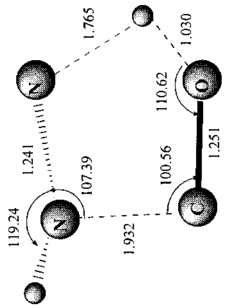

TSi$_3$P$_8$ (^{3}A, C$_1$)

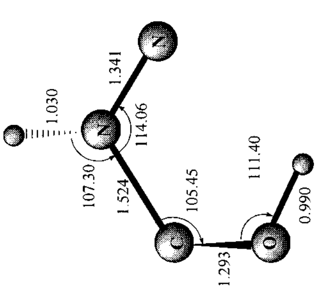

TSi$_3$j$_4$ (^{3}A, C$_1$)

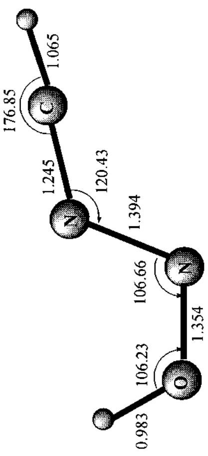

TSk$_2$k$_8$ (^{3}A'', C$_s$)

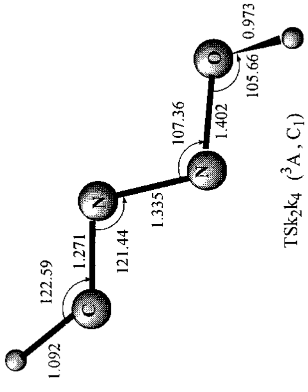

TSk$_2$k$_4$ (^{3}A, C$_1$)

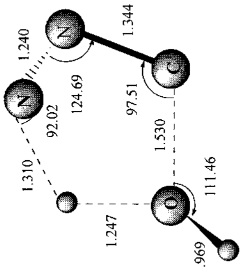

TSj$_3$P$_{11}$ (^{3}A, C$_1$)

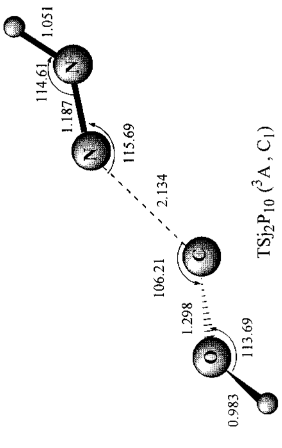

TSj$_2$P$_{10}$ (^{3}A, C$_1$)

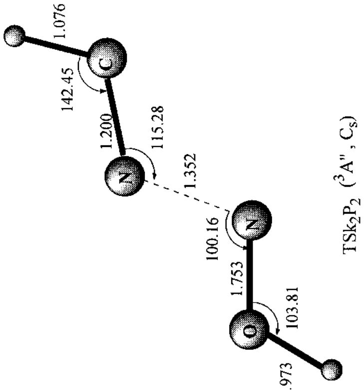

TSk$_2$P$_2$ (^{3}A'', C$_s$)

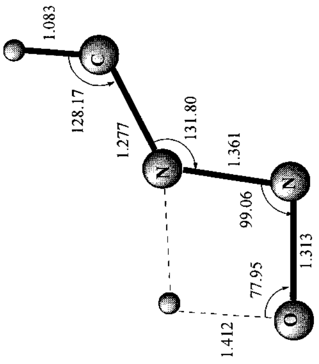

TSk$_2$m$_2$ (^{3}A'', C$_s$)

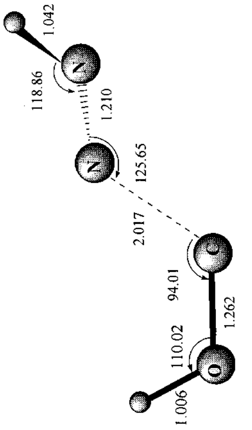

TSj$_6$P$_{10}$ (^{3}A, C$_1$)

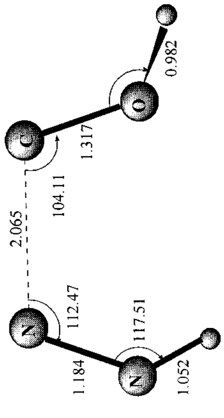

TSj$_3$P$_{10}$ (^{3}A, C$_1$)

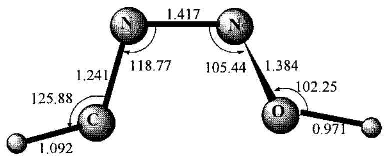

TSk$_3$k$_4$ (^{3}A , C$_1$)

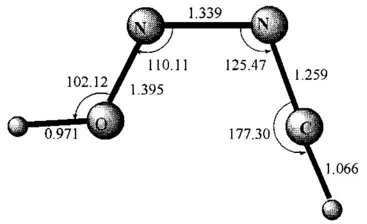

TSk$_3$k$_5$ (^{3}A" , C$_s$)

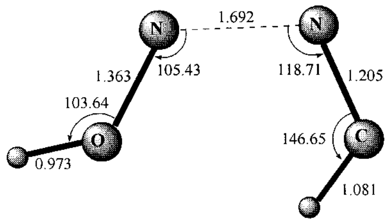

TSk$_5$P$_2$ (^{3}A , C$_1$)

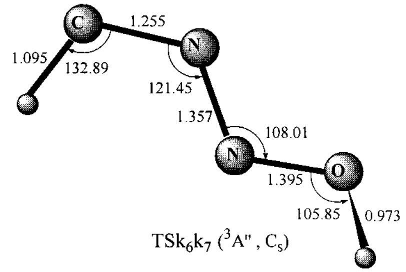

TSk$_6$k$_7$ (^{3}A" , C$_s$)

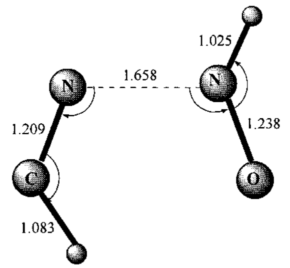

TSk$_3$P$_2$ (^{3}A , C$_1$)

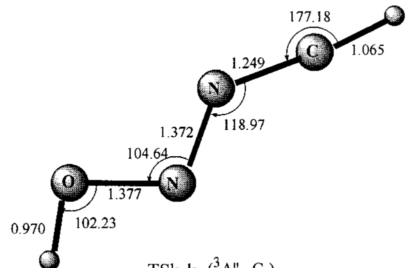

TSk$_4$k$_6$ (^{3}A" , C$_s$)

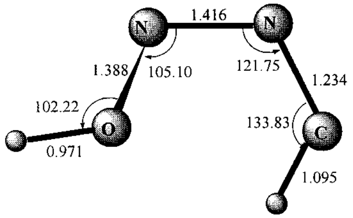

TSk$_6$k$_8$ (^{3}A , C$_1$)

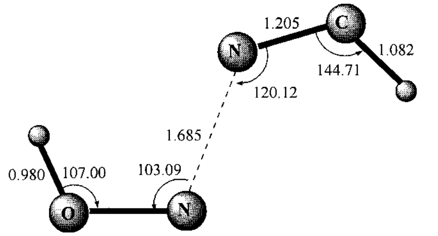

TSk$_6$P$_2$ (^{3}A" , C$_s$)

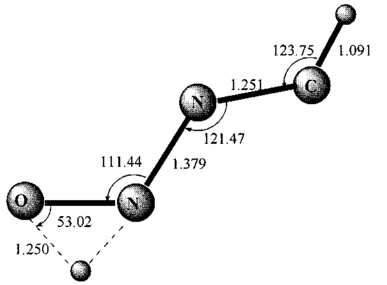

TSk$_4$l$_2$ (^{3}A , C$_1$)

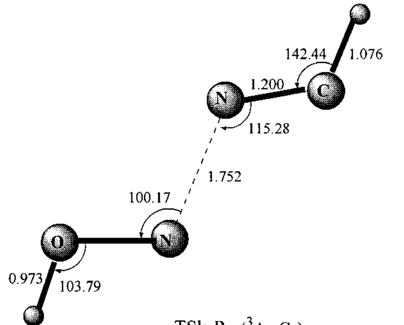

TSk$_4$P$_2$ (^{3}A , C$_1$)

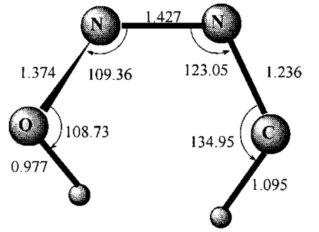

TSk$_7$k$_8$ (^{3}A , C$_1$)

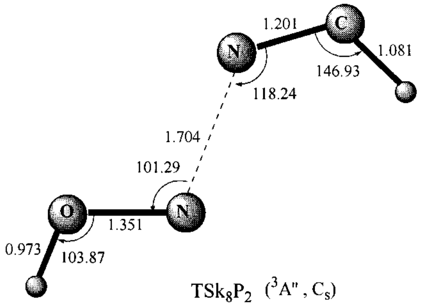

TSk$_8$P$_2$ (^{3}A" , C$_s$)

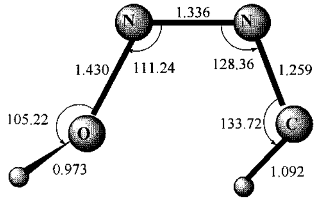

TSk$_5$k$_7$ (^{3}A , C$_1$)

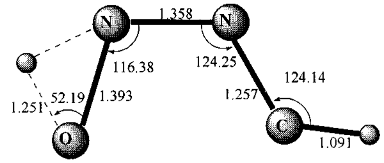

TSk$_5$l$_3$ (^{3}A , C$_1$)

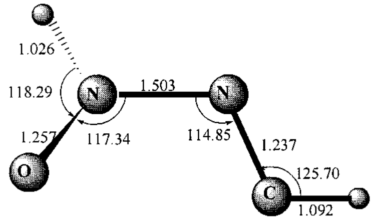

TSl$_1$l$_2$ (^{3}A , C$_1$)

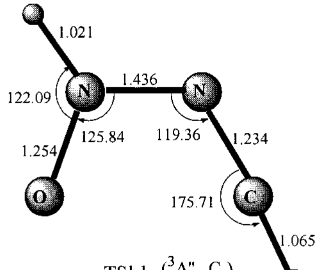

TSl$_1$l$_3$ (^{3}A" , C$_s$)

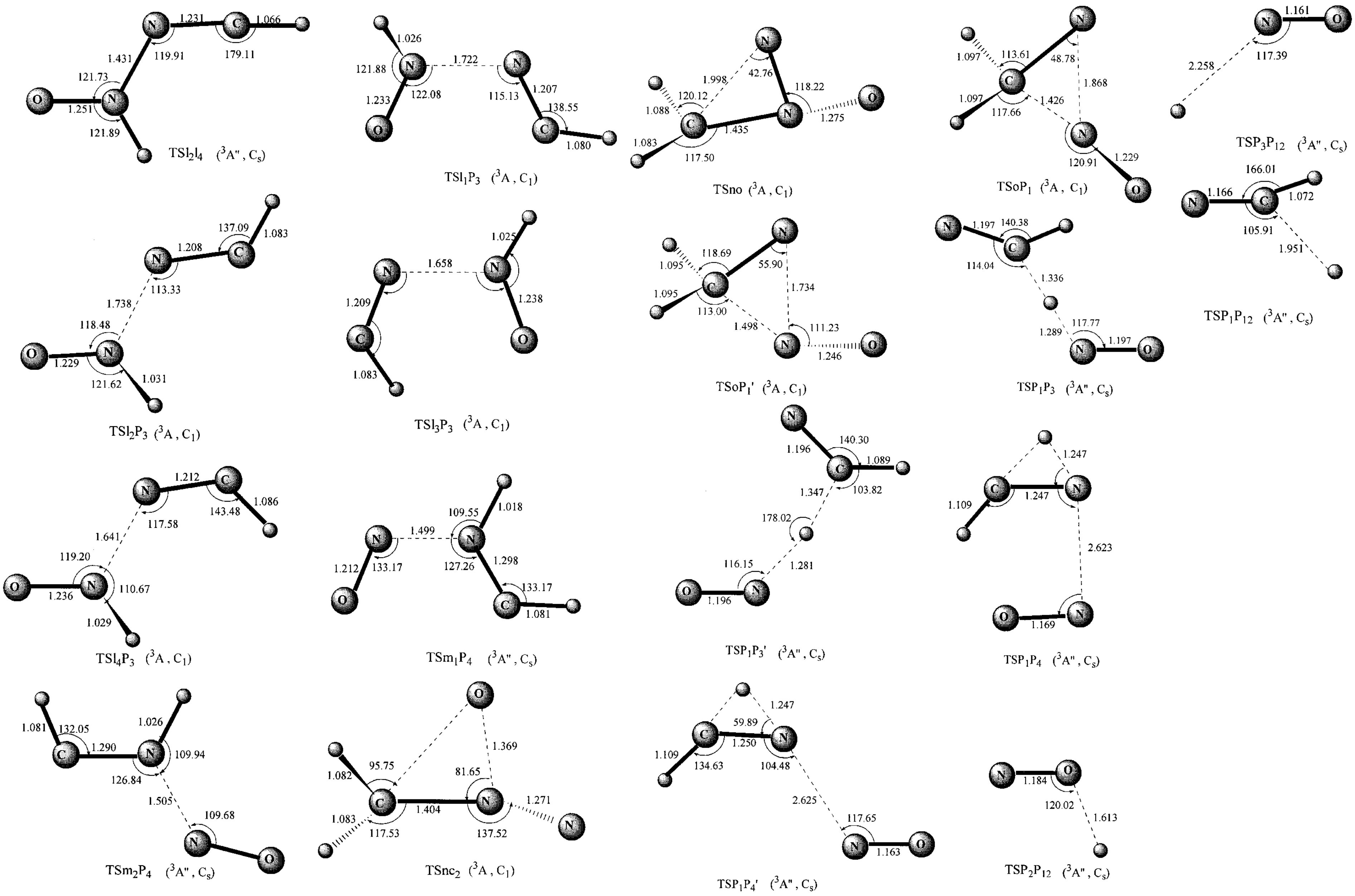

TSI$_2$I$_4$ (^{3}A", C$_s$)

TSI$_1$P$_3$ (^{3}A, C$_1$)

TSno (^{3}A, C$_1$)

TSoP$_1$ (^{3}A, C$_1$)

TSP$_3$P$_{12}$ (^{3}A", C$_s$)

TSP$_1$P$_{12}$ (^{3}A", C$_s$)

TSI$_2$P$_3$ (^{3}A, C$_1$)

TSI$_3$P$_3$ (^{3}A, C$_1$)

TSoP$_1$' (^{3}A, C$_1$)

TSP$_1$P$_3$ (^{3}A", C$_s$)

TSI$_4$P$_3$ (^{3}A, C$_1$)

TSm$_1$P$_4$ (^{3}A", C$_s$)

TSP$_1$P$_3$' (^{3}A", C$_s$)

TSP$_1$P$_4$ (^{3}A", C$_s$)

TSm$_2$P$_4$ (^{3}A", C$_s$)

TSnc$_2$ (^{3}A, C$_1$)

TSP$_1$P$_4$' (^{3}A", C$_s$)

TSP$_2$P$_{12}$ (^{3}A", C$_s$)

Figure 3. B3LYP/6-31G(d,p)-optimized geometries of all transition states. Bond distances are in Å, and angles are in deg.

TABLE 1: Zero-Point, Total (au), and Relative Energies in Parentheses (kcal/mol) as well as Those including Zero-Point Vibration Energies (kcal/mol) of Reactants and Products for the $^3CH_2 + N_2O$ Reaction at the B3LYP/6-31G(d,p) Level and the QCISD(T)/6-311G(d,p)//B3LYP/6-31G(d,p)+ZPE Level

species	ZPE	B3LYP	QCISD(T)	QCISD(T) + ZPE
R ($^3CH_2 + N_2O$)	0.028586	−223.813760 (0.0)	−223.348852 (0.0)	0.0
$\mathbf{P_1}$ ($H_2CN + NO$)	0.029820	−223.873579 (−37.5)	−223.406671 (−36.3)	−35.5
$\mathbf{P_2}$ ($HCN + {}^3HON$)	0.030196	−223.863819 (−31.4)	−223.400713 (−32.5)	−31.5
$\mathbf{P_3}$ ($HCN + {}^3HNO$)	0.030061	−223.879012 (−40.9)	−223.409260 (−37.9)	−37.0
$\mathbf{P_4}$ ($HCNH + NO$)	0.029442	−223.850219 (−22.9)	−223.383412 (−21.7)	−21.1
$\mathbf{P_5}$ ($^3H_2CO + N_2$)	0.028991	−223.919608 (−66.4)	−223.456503 (−66.4)	−67.3
$\mathbf{P_6}$ ($^3HCOH + N_2$)	0.030109	−223.903512 (−56.3)	−223.447991 (−62.2)	−61.3
$\mathbf{P_7}$ ($^3H_2NN + CO$)	0.031315	−223.897982 (−52.9)	−223.439029 (−56.6)	−54.9
$\mathbf{P_8}$ ($^3HNNH + CO$)	0.029891	−223.894849 (−50.9)	−223.429370 (−50.5)	−49.7
$\mathbf{P_9}$ ($N_2H + HCO$)	0.026292	−223.884557 (−44.4)	−223.415527 (−41.8)	−43.3
$\mathbf{P_{10}}$ ($N_2H + HOC$)	0.026393	−223.816906 (−2.0)	−223.349519 (−0.4)	−1.8
$\mathbf{P_{11}}$ ($H_2O + {}^3CN_2$)	0.029618	−223.864755 (−32.0)	−223.397174 (−30.3)	−29.7
$\mathbf{P_{12}}$ ($HCN + NO + H$)	0.021005	−223.806345 (4.7)	−223.362271 (−8.4)	−13.2

TABLE 2: Zero-Point, Total (au), and Relative Energies in Parentheses (kcal/mol) as well as Those including Zero-point Vibration Energies (kcal/mol) of the Isomers for the $^3CH_2 + N_2O$ Reaction at the B3LYP/6-31G(d,p) Level and the QCISD(T)/6-311G(d,p)//B3LYP/6-31G(d,p)+ZPE Level

species	ZPE	B3LYP	QCISD(T)	QCISD(T) + ZPE
$\mathbf{a_1}$	0.035981	−223.877891 (−40.2)	−223.389772 (−25.7)	−21.0
$\mathbf{a_2}$	0.035947	−223.885854 (−45.2)	−223.394118 (−28.4)	−23.8
b	0.036531	−223.807712 (3.8)	−223.324845 (15.1)	20.1
$\mathbf{c_1}$	0.033852	−223.893007 (−49.7)	−223.413263 (−40.4)	−37.1
$\mathbf{c_2}$	0.033707	−223.893025 (−49.7)	−223.413261 (−40.4)	−37.2
$\mathbf{d_1}$	0.036831	−223.920497 (−67.0)	−223.440429 (−57.5)	−52.3
$\mathbf{d_2}$	0.036862	−223.924213 (−69.3)	−223.443442 (−59.4)	−54.2
$\mathbf{e_1}$	0.036165	−223.918098 (−65.5)	−223.429050 (−50.3)	−45.6
$\mathbf{e_2}$	0.035434	−223.917108 (−64.9)	−223.428458 (−50.0)	−45.7
$\mathbf{e_3}$	0.035271	−223.912736 (−62.1)	−223.422593 (−46.3)	−42.1
$\mathbf{e_4}$	0.034415	−223.906123 (−58.0)	−223.415243 (−41.7)	−38.0
$\mathbf{f_1}$	0.037683	−223.907951 (−59.1)	−223.427451 (−49.3)	−43.6
$\mathbf{f_2}$	0.037657	−223.913909 (−62.8)	−223.431842 (−52.1)	−46.4
$\mathbf{f_3}$	0.038257	−223.915690 (64.0)	−223.434567 (−53.8)	−47.7
$\mathbf{f_4}$	0.037236	−223.909232 (−59.9)	−223.427839 (−49.6)	−44.3
$\mathbf{g_1}$	0.037268	−223.914329 (−63.1)	−223.431542 (−51.9)	−46.4
$\mathbf{g_2}$	0.036551	−223.918430 (−65.7)	−223.435123 (−51.1)	−49.1
$\mathbf{h_1}$	0.036522	−223.922518 (−68.2)	−223.440262 (−57.4)	−52.4
$\mathbf{h_2}$	0.036237	−223.922626 (−68.3)	−223.440178 (−57.3)	−52.5
$\mathbf{h_3}$	0.037126	−223.930113 (−73.0)	−223.447629 (−62.0)	−56.6
$\mathbf{h_4}$	0.036670	−223.929377 (−72.6)	−223.446852 (−61.5)	−56.4
$\mathbf{i_1}$	0.036852	−223.856527 (−26.8)	−223.382628 (−21.2)	−16.0
$\mathbf{i_2}$	0.036308	−223.856356 (−26.7)	−223.382919 (−21.4)	−16.5
$\mathbf{i_3}$	0.035950	−223.851601 (−23.7)	−223.375496 (−16.7)	−12.1
$\mathbf{i_4}$	0.035150	−223.845849 (−20.1)	−223.370658 (−13.7)	−9.6
$\mathbf{j_1}$	0.035798	−223.868762 (−34.5)	−223.385651 (−23.1)	−18.6
$\mathbf{j_2}$	0.036539	−223.879858 (−41.5)	−223.396008 (−29.6)	−24.6
$\mathbf{j_3}$	0.034851	−223.860424 (−29.3)	−223.379081 (−19.0)	−15.0
$\mathbf{j_4}$	0.035994	−223.874090 (−37.9)	−223.390234 (−26.0)	−21.3
$\mathbf{j_5}$	0.036335	−223.872815 (−37.1)	−223.392106 (−27.1)	−22.3
$\mathbf{j_6}$	0.035675	−223.874006 (−37.8)	−223.390231 (−26.0)	−21.5
$\mathbf{j_7}$	0.034052	−223.853117 (−24.7)	−223.371352 (−14.1)	−10.7
$\mathbf{j_8}$	0.036119	−223.878480 (−40.6)	−223.394853 (−28.9)	−24.1
$\mathbf{k_1}$	0.034838	−223.837564 (−14.9)	−223.354725 (−3.7)	0.2
$\mathbf{k_2}$	0.034868	−223.840979 (−17.1)	−223.358693 (−6.2)	−2.2
$\mathbf{k_3}$	0.035168	−223.839743 (−16.3)	−223.357945 (−5.7)	−1.6
$\mathbf{k_4}$	0.035174	−223.840697 (−16.9)	−223.358838 (−6.3)	−2.1
$\mathbf{k_5}$	0.034404	−223.832435 (−11.7)	−223.339722 (5.7)	9.4
$\mathbf{k_6}$	0.034625	−223.834663 (−13.1)	−223.352683 (−2.4)	1.4
$\mathbf{k_7}$	0.033113	−223.821898 (−5.1)	−223.338726 (6.4)	9.2
$\mathbf{k_8}$	0.034354	−223.836316 (−14.2)	−223.353944 (−3.2)	0.4
$\mathbf{l_1}$	0.035892	−223.843203 (−18.5)	−223.356928 (−5.1)	−0.5
$\mathbf{l_2}$	0.035214	−223.840058 (−16.5)	−223.353151 (−2.7)	1.5
$\mathbf{l_3}$	0.034455	−223.832113 (−11.5)	−223.344583 (2.7)	6.4
$\mathbf{l_4}$	0.035210	−223.839459 (−16.1)	−223.353119 (−2.7)	1.5
$\mathbf{m_1}$	0.033545	−223.815879 (−1.3)	−223.331876 (10.7)	13.8
$\mathbf{m_2}$	0.032781	−223.814825 (−0.7)	−223.329080 (12.4)	15.0
n	0.034417	−223.830055 (−10.2)	−223.344895 (2.5)	6.1
o	0.035815	−223.818025 (−2.7)	−223.331296 (11.0)	15.6

4 (for $\mathbf{P_1}-\mathbf{P_4}$ and $\mathbf{P_{12}}$) and Figure 5 (for $\mathbf{P_5}-\mathbf{P_{11}}$). Unless otherwise specified, the energies in the following discussions are referred to as the QCISD(T)/6-311G(d,p)//B3LYP/6-31G(d,p)+ZPE values.

TABLE 3: Zero-Point, Total (au), and Relative Energies in Parentheses (kcal/mol) as well as Those including Zero-Point Vibration Energies (kcal/mol) of the Transition States for the $^3CH_2 + N_2O$ Reaction at the B3LYP/6-31G(d,p) Level and the QCISD(T)/6-311G(d,p)//B3LYP/6-31G(d,p)+ZPE Level

species	ZPE	B3LYP	QCISD(T)	QCISD(T) + ZPE	species	ZPE	B3LYP	QCISD(T)	QCISD(T) + ZPE
TSRa$_1$	0.029888	−223.802946(6.8)	−223.326620(14.0)	14.8	**TSh$_3$P$_6$**	0.032844	−223.891657(−48.9)	−223.419105(−44.1)	−41.4
TSRn	0.030890	−223.784381(18.4)	−223.306260(26.7)	28.2	**TSh$_4$j$_6$**	0.031219	−223.824258(−6.6)	−223.344681(2.6)	4.3
TSRP$_5$	0.029626	−223.787695(16.4)	−223.307646(25.9)	26.5	**TSh$_4$P$_6$**	0.032193	−223.889562(−47.6)	−223.417929(−43.3)	−41.1
TSRP$_5$′	0.029542	−223.760725(33.3)	−223.275122(46.3)	46.9	**TSi$_1$i$_2$**	0.035020	−223.814912(−0.7)	−223.342377(4.0)	8.1
TSa$_1$a$_2$	0.035136	−223.862140(−30.4)	−223.377479(−18.0)	−13.9	**TSi$_1$i$_3$**	0.033713	−223.829219(−9.7)	−223.353003(−2.6)	0.6
TSa$_1$b	0.034661	−223.787805(16.3)	−223.303561(28.4)	32.3	**Tsi$_1$j$_1$**	0.030456	−223.775853(23.8)	−223.296356(32.9)	34.1
TSa$_1$k$_1$	0.030506	−223.819311(−3.5)	−223.332441(10.3)	11.6	**TSi$_2$i$_4$**	0.033334	−223.828001(−8.9)	−223.353409(−2.9)	0.1
TSa$_2$l$_2$	0.029293	−223.773331(25.4)	−223.286025(39.4)	39.9	**Tsi$_2$j$_2$**	0.030430	−223.789723(−15.1)	−223.308715(25.2)	26.3
TSa$_2$n	0.031651	−223.742468(44.7)	−223.257377(57.4)	59.3	**TSi$_2$P$_{10}$**	0.030674	−223.811927(1.2)	−223.334518(9.0)	10.3
TSa$_1$P$_1$	0.032978	−223.858750(−28.2)	−223.375022(−16.4)	−13.7	**TSi$_3$i$_4$**	0.034307	−223.817654(−2.4)	−223.344595(2.7)	6.3
TSa$_2$P$_1$	0.032931	−223.865020(−32.2)	−223.382698(−21.2)	−18.5	**TSi$_3$P$_8$**	0.031584	−223.822842(−5.7)	−223.342310(4.1)	6.0
TSbc$_1$	0.035219	−223.802445(7.1)	−223.320844(−17.6)	21.7	**TSj$_2$P$_{10}$**	0.030233	−223.814922(−0.7)	−223.339885(5.6)	6.7
TSc$_1$c$_2$	0.033224	−223.890992(−48.5)	−223.411323(−39.2)	−36.3	**TSj$_3$P$_{10}$**	0.029799	−223.801515(7.7)	−223.320814(17.6)	19.0
TSc$_1$d$_1$	0.028015	−223.839878(−16.4)	−223.356580(−4.8)	−5.2	**TSj$_3$P$_{10}$**	0.031301	−223.815770(−1.3)	−223.340089(5.5)	7.0
TSc$_1$h$_1$	0.030644	−223.841190(−17.2)	−223.359286(−6.5)	−5.3	**TSj$_6$P$_{10}$**	0.031021	−223.819670(−3.7)	−223.338239(6.7)	8.0
TSc$_1$P$_5$	0.032583	−223.892698(−49.5)	−223.412605(−40.0)	−37.5	**TSk$_1$k$_2$**	0.033878	−223.821935(−5.1)	−223.341744(4.5)	7.8
TSc$_2$d$_2$	0.027588	−223.837647(−15.0)	−223.354093(−3.3)	−3.9	**TSk$_1$k$_3$**	0.033051	−223.821987(−5.2)	−223.340729(5.1)	7.9
TSc$_2$h$_2$	0.030288	−223.841395(−17.3)	−223.359252(−6.5)	−5.5	**TSk$_1$k$_7$**	0.031556	−223.813036(0.5)	−223.329235(12.3)	14.2
TSc$_2$P$_5$	0.032218	−223.892484(−49.4)	−223.409566(−38.1)	−35.8	**TSk$_1$P$_2$**	0.031926	−223.818099(−2.7)	−223.337771(7.0)	9.1
TSd$_1$d$_2$	0.035568	−223.894007(−50.4)	−223.418872(−43.9)	−39.6	**TSk$_2$k$_4$**	0.033045	−223.823329(−6.0)	−223.342036(4.3)	4.6
TSd$_1$e$_1$	0.031091	−223.845365(−19.8)	−223.363834(−9.4)	−7.8	**TSk$_2$k$_8$**	0.032066	−223.819878(−3.8)	−223.336563(7.7)	9.9
TSd$_1$i$_1$	0.030766	−223.795226(11.6)	−223.315608(21.0)	22.2	**TSk$_2$m$_2$**	0.031204	−223.787117(16.7)	−223.270924(48.9)	50.5
TSd$_1$P$_9$	0.031151	−223.878390(−40.6)	−223.397379(−30.5)	−28.8	**TSk$_2$P$_2$**	0.031902	−223.822418(−5.4)	−223.342615(3.9)	4.4
TSd$_2$e$_2$	0.030726	−223.845186(−17.2)	−223.363177(−9.0)	−7.7	**TSk$_3$k$_4$**	0.034506	−223.825481(−7.4)	−223.346472(1.5)	5.2
TSd$_2$f$_2$	0.031967	−223.856630(−26.9)	−223.373723(−15.6)	−13.5	**TSk$_3$P$_2$**	0.031613	−223.813347(0.3)	−223.334731(8.9)	10.8
TSd$_2$h$_4$	0.031560	−223.870121(−35.4)	−223.381976(−20.8)	−18.9	**TSk$_3$k$_5$**	0.032205	−223.816211(−1.5)	−223.333322(9.7)	12.0
TSd$_2$i$_2$	0.030438	−223.797551(10.2)	−223.317568(19.6)	20.8	**TSk$_4$k$_6$**	0.032436	−223.817130(−2.1)	−223.334558(9.0)	11.4
TSd$_2$P$_9$	0.031013	−223.878966(−40.9)	−223.397605(−30.6)	−29.1	**TSk$_4$l$_2$**	0.029166	−223.759349(34.1)	−223.274640(46.6)	46.9
TSe$_1$e$_2$	0.034865	−223.904950(−57.2)	−223.420466(−44.9)	−41.0	**TSk$_4$P$_2$**	0.031788	−223.816503(−1.7)	−223.337651(7.0)	9.0
TSe$_1$f$_1$	0.029184	−223.826304(−7.9)	−223.339148(6.1)	6.5	**TSk$_5$k$_7$**	0.032308	−223.814453(−0.4)	−223.333044(9.9)	12.3
TSe$_1$f$_3$	0.029572	−223.817536(−2.4)	−223.332536(10.2)	10.9	**TSk$_5$l$_3$**	0.029444	−223.757577(35.3)	−223.273319(47.4)	47.9
TSe$_1$j$_1$	0.029589	−223.808424(3.3)	−223.321975(16.9)	17.5	**TSk$_5$P$_2$**	0.031900	−223.817904(−2.6)	−223.339727(5.7)	7.8
TSe$_1$P$_9$	0.030746	−223.881097(−42.3)	−223.400289(−32.3)	−30.9	**TSk$_6$k$_7$**	0.034133	−223.822969(−5.8)	−223.343072(3.6)	7.1
TSe$_2$g$_2$	0.029747	−223.850517(−23.1)	−223.362364(−8.5)	−7.8	**TSk$_6$k$_8$**	0.032433	−223.818036(−2.7)	−223.336575(7.7)	10.1
TSe$_2$j$_2$	0.030184	−223.820487(−4.2)	−223.331573(10.8)	11.8	**TSk$_6$P$_2$**	0.032064	−223.820610(−4.3)	−223.341774(4.4)	6.6
TSe$_2$P$_9$	0.030434	−223.879804(−41.4)	−223.399380(−31.7)	−30.6	**TSk$_7$k$_8$**	0.033440	−223.818837(−3.2)	−223.337774(6.9)	10.0
TSe$_3$h$_3$	0.032532	−223.886303(−45.5)	−223.398466(−31.1)	−28.7	**TSk$_8$P$_2$**	0.032161	−223.826509(−8.0)	−223.346735(1.3)	3.6
TSe$_3$j$_3$	0.028842	−223.800396(8.4)	−223.314965(21.3)	21.4	**TSl$_1$l$_2$**	0.034567	−223.827440(−8.6)	−223.343096(3.6)	4.9
TSe$_4$j$_4$	0.029567	−223.813281(0.3)	−223.323996(15.6)	16.2	**TSl$_1$l$_3$**	0.032503	−223.825044(−7.1)	−223.337709(7.0)	9.5
TSf$_1$f$_4$	0.035349	−223.878239(−40.5)	−223.402100(−33.4)	−29.2	**TSl$_1$P$_3$**	0.032565	−223.829661(−10.0)	−223.344406(2.8)	5.3
TSf$_1$f$_3$	0.034989	−223.860704(−29.5)	−223.360749(−7.5)	−3.4	**TSl$_2$l$_4$**	0.031893	−223.820395(−4.2)	−223.332345(10.4)	12.4
TSf$_1$P$_8$	0.032996	−223.873517(−37.5)	−223.395940(−29.5)	−26.8	**TSl$_2$P$_3$**	0.032106	−223.827065(−8.3)	−223.341077(4.9)	7.1
TSf$_2$f$_3$	0.035747	−223.882869(−43.4)	−223.405220(−35.4)	−30.9	**TSl$_3$P$_3$**	0.032659	−223.833115(−12.1)	−223.347963(0.6)	3.1
TSf$_2$g$_2$	0.030770	−233.825631(−7.5)	−223.344451(2.8)	4.1	**TSl$_4$P$_3$**	0.032125	−223.826640(−8.1)	−223.340438(5.3)	7.5
TSf$_2$P$_8$	0.032712	−223.879324(−41.1)	−223.400538(−32.4)	−29.9	**TSm$_1$P$_4$**	0.031816	−223.815323(−1.0)	−223.328904(12.5)	14.5
TSf$_3$g$_1$	0.031293	−223.833619(−12.5)	−223.342414(4.0)	5.7	**TSm$_2$P$_4$**	0.031204	−223.814131(−0.2)	−223.326379(14.1)	15.7
TSf$_3$i$_3$	0.031519	−223.829679(−10.0)	−223.348857(0.0)	1.8	**TSnc$_2$**	0.033015	−223.765190(30.5)	−223.275694(45.9)	48.7
TSf$_3$P$_8$	0.033135	−223.881790(−42.7)	−223.403443(−34.2)	−31.4	**TSno**	0.033733	−223.772632(25.8)	−223.284190(40.6)	43.8
TSf$_4$P$_8$	0.032650	−223.872397(−36.8)	−223.394607(−28.7)	−26.2	**TSoP$_1$**	0.034074	−223.802156(7.3)	−223.320906(17.5)	21.0
TSg$_1$g$_2$	0.036094	−223.895046(−51.0)	−223.415401(−41.8)	−37.0	**TSoP$_1$′**	0.033067	−223.804695(5.7)	−223.310057(24.3)	27.2
TSg$_1$P$_7$	0.033823	−223.885260(−44.9)	−223.411400(−39.2)	−36.0	**TSP$_1$P$_3$**	0.026267	−223.848196(−21.6)	−223.364635(−9.9)	−11.4
TSg$_2$P$_7$	0.033974	−223.892965(−49.7)	−223.421101(−45.3)	−42.0	**TSP$_1$P$_3$′**	0.026099	−223.847258(−21.0)	−223.363845(−9.4)	−11.0
TSh$_1$h$_3$	0.034786	−223.913391(−62.5)	−223.432270(−52.3)	−48.5	**TSP$_1$P$_4$**	0.025592	−223.795114(11.7)	−223.328265(12.9)	11.0
TSh$_1$i$_1$	0.030255	−223.797105(10.5)	−223.317332(19.8)	20.8	**TSP$_1$P$_4$′**	0.026276	−223.796176(11.0)	−223.327482(13.4)	12.0
TSh$_2$h$_4$	0.034476	−223.913392(−62.5)	−223.432257(−52.3)	−48.6	**TSP$_1$P$_{12}$**	0.027655	−223.832351(−11.7)	−223.362825(−8.8)	−9.4
TSh$_2$j$_4$	0.031336	−223.824779(−6.9)	−223.345202(2.3)	0.2	**TSP$_2$P$_{12}$**	0.021757	−223.804897(5.6)	−223.342583(3.9)	−0.4
TSh$_3$i$_3$	0.029897	−223.795002(11.8)	−223.314520(21.5)	22.4	**TSP$_3$P$_{12}$**	0.021396	−223.813377(0.2)	−223.359347(−6.6)	−11.1

For the initial step of the title reaction, we consider five possible attack ways of $^3CH_2$ at N_2O, i.e., end-N attack, end-O attack, middle-N attack, N−N π bonding attack, and N−O π bonding attack. There is an end-N attack transition state **TSRa$_1$** linking the reactants **R** ($^3CH_2 + N_2O$) with the chainlike isomer *cis*-H_2CNNO (**a$_1$**) after overcoming a considerable barrier of 14.8 kcal/mol. The conversion from **a$_1$** to its trans from (**a$_2$**) is very easy, with a low barrier of 7.1 kcal/mol. Note that the transition state **TSRa$_2$** cannot be obtained. The end-O attack can directly lead to product **P$_5$** ($^3H_2CO + N_2$) either via a cis transition state **TSRP$_5$** or a trans **TSRP$_5$′** with the much larger barriers of 26.5 and 46.9 kcal/mol, respectively. Surely, the cis end-O attack is much more favorable than the trans end-O attack. The middle-N attack can be realized via **TSRn**, with a barrier of 28.2 kcal/mol leading to the branched-isomer ($H_2CN(O)N$) **n**. We cannot find any transition states that are directly associated with the N−N and N−O π bonding attack. The search for such transition states often leads to **TSRn** or **TSRa$_1$**. It is also worth noting that the search for the direct N-abstraction transition state between $^3CH_2$ and N_2O usually leads to **TSRa$_1$** or **TSa$_1$P$_1$** (or **TSa$_2$P$_1$**). Surely, we can find from Figure 4 and Figure 5 that the end-N attack is the most favorable association channel for the title reaction. For simplicity, we mainly discuss the formation pathways of various products proceeded via **a**.

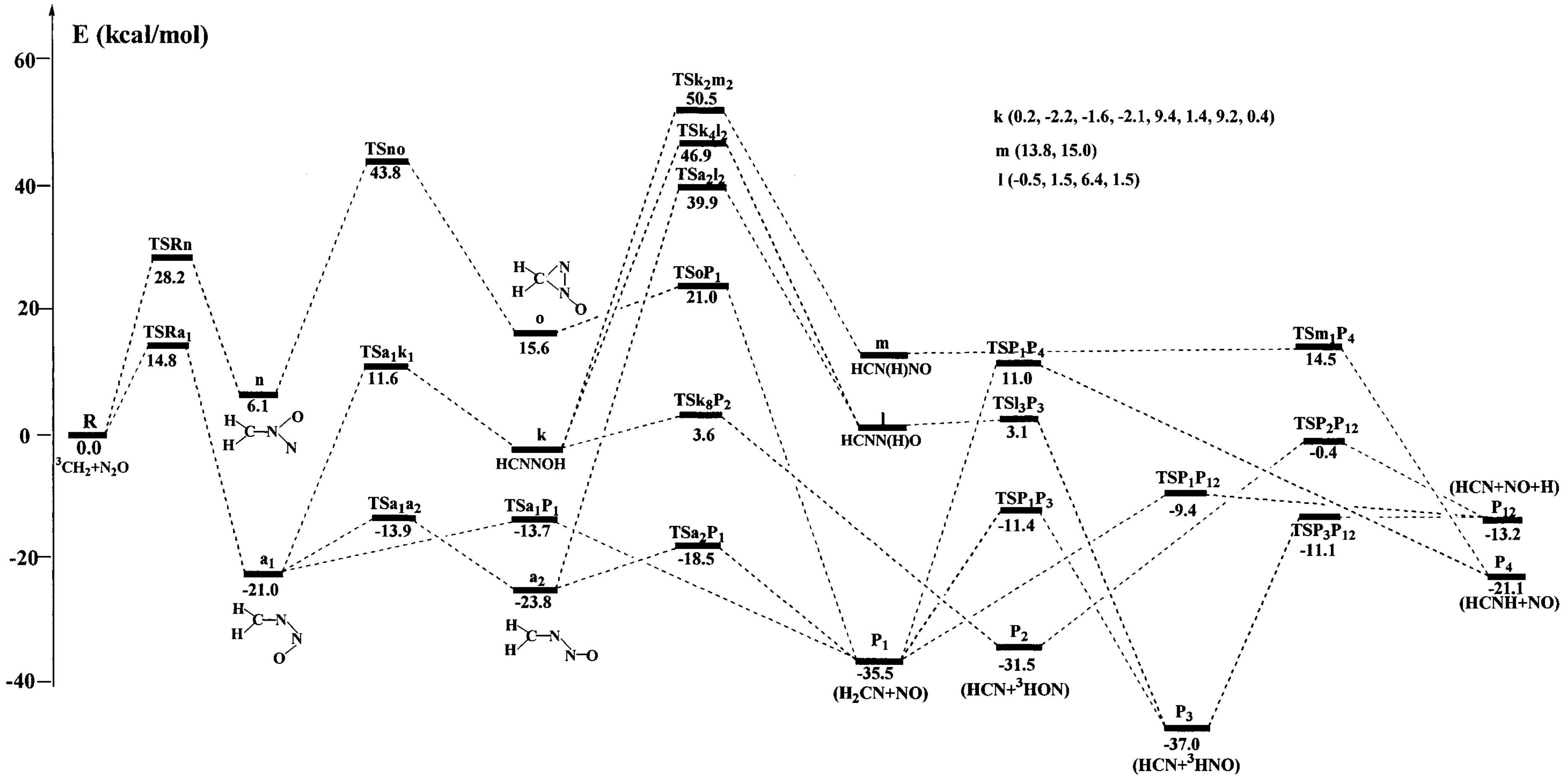

Figure 4. Schematic reaction pathways for **P**$_1$−**P**$_4$ and **P**$_{12}$ for the $^3CH_2 + N_2O$ reaction at the QCISD(T)/6-311G(d,p)//B3LYP/6-31G(d,p)+ZPE level. The relative energies of various isomeric forms of **l** and **m** are given in sequence in parentheses.

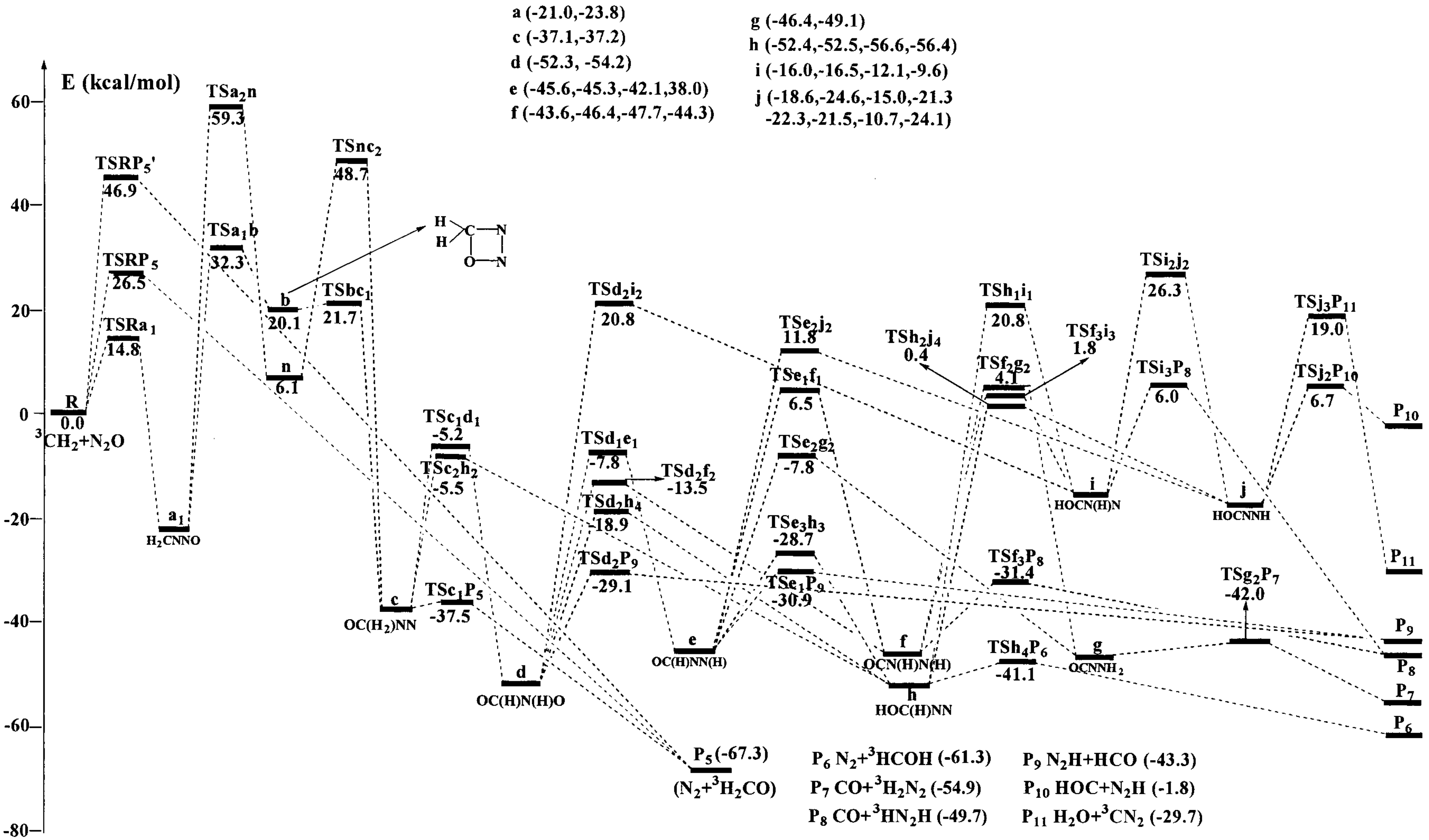

Figure 5. Schematic reaction pathways for $\mathbf{P_5}$−$\mathbf{P_{11}}$ for the $^3CH_2$ + N_2O reaction at the QCISD(T)/6-311G(d,p)//B3LYP/6-31G(d,p)+ZPE level. The relative energies of various isomeric forms of **a** and **c**−**j** are given in sequence in parentheses.

3.1. Formation of $\mathbf{P_1}$ ($\mathbf{H_2CN + NO}$), $\mathbf{P_2}$ ($\mathbf{HCN + {}^3HON}$), and $\mathbf{P_{12}}$ ($\mathbf{HCN + NO + H}$). As shown in Figure 4, the initially formed end-N attack isomer H_2CNNO ($\mathbf{a_1}$) can directly dissociate to $\mathbf{P_1}$ ($H_2CN + NO$) via the N−N bond cleavage or isomerize to its trans form $\mathbf{a_2}$, with $\mathbf{a_2}$ then undergoing a direct N−N bond cleavage to form $\mathbf{P_1}$. The direct dissociation of $\mathbf{a_1}$ and $\mathbf{a_2}$ is barrier-consumed processes, i.e., 7.3 kcal/mol via $\mathbf{TSa_1P_1}$ and 5.3 via kcal/mol $\mathbf{TSa_2P_1}$. Such processes can be described as:

$$\text{Path P}_1\text{:}\qquad \mathbf{R} \rightarrow \mathbf{a}\ (\mathbf{a_1}, \mathbf{a_2}) \rightarrow \mathbf{P_1}\ (\mathbf{H_2CN + NO})$$

The formation of $\mathbf{P_1}$ from the initially formed middle-N attack isomer ($H_2CN(O)N$) $\mathbf{n}$ seems unlikely due to the high-energy of the involved **TSno** (43.8 kcal/mol above **R**).

The isomer (H_2CNNO) $\mathbf{a_1}$ can alternatively undergoes a 1,4-H shift via $\mathbf{TSa_1k_1}$ to form the chainlike isomer (HCNNOH) $\mathbf{k_1}$. $\mathbf{k_1}$ can then dissociate to $\mathbf{P_2}$ ($HCN + {}^3HON$) via $\mathbf{TSk_1P_2}$ also through the direct N−N rupture. Interestingly, there are altogether 8 isomers ($\mathbf{k_1 - k_8}$) for the HCNNOH structure that can be interconverted between each other via 11 transition states: $\mathbf{TSk_1k_2}$, $\mathbf{TSk_1k_3}$, $\mathbf{TSk_1k_7}$, $\mathbf{TSk_2k_4}$, $\mathbf{TSk_3k_4}$, $\mathbf{TSk_3k_5}$, $\mathbf{TSk_4k_6}$, $\mathbf{TSk_5k_7}$, $\mathbf{TSk_6k_7}$, $\mathbf{TSk_6k_8}$, and $\mathbf{TSk_7k_8}$. Except $\mathbf{k_7}$, all isomers can each lead to $\mathbf{P_2}$ via a direct dissociation transition state. Note that the relative energies of $\mathbf{TSk_6k_7}$ and $\mathbf{TSk_5P_2}$ are abnormal, i.e., 2.1 and 1.6 kcal/mol lower than $\mathbf{k_6}$ and $\mathbf{k_5}$, respectively, which can surely be ascribed to the single-point energy calculations. The formation pathways of $\mathbf{P_2}$ via $\mathbf{a_1}$ and **k** are written as:

$$\text{Path P}_2\text{:}\qquad \mathbf{R} \rightarrow \mathbf{a_1} \rightarrow \mathbf{k}\ (\mathbf{k_1} - \mathbf{k_8}) \rightarrow \mathbf{P_2}\ (\mathbf{HCN + {}^3HON})$$

The energies of all intermediates and transition states involved in **Path P$_1$** and **Path P$_2$** are lower than that of the entrance $\mathbf{TSRa_1}$. Then, both **Path P$_1$** and **Path P$_2$** may be energetically accessible once $\mathbf{a_1}$ is formed. Since the barrier for $\mathbf{a_1} \rightarrow \mathbf{k_1}$ (32.6 kcal/mol) in **Path P$_2$** is significantly larger than those for $\mathbf{a_1} \rightarrow \mathbf{P_1}$ (7.3 kcal/mol) and $\mathbf{a_1} \rightarrow \mathbf{a_2}$ (7.1 kcal/mol) in **Path P$_1$**, **Path P$_2$** is certainly much less competitive than **Path P$_1$**.

The released energy from $\mathbf{TSRa_1}$ to $\mathbf{P_1}$ ($H_2CN + NO$) and $\mathbf{P_2}$ ($HCN + {}^3HON$) may further drive their secondary dissociation to the same product $\mathbf{P_{12}}$ ($HCN + NO + H$) with relatively high energy (−13.2 kcal/mol below **R**), i.e., via the direct C−H cleavage of H_2CN in $\mathbf{P_1}$ and via the direct O−H cleavage of ${}^3HON$ in $\mathbf{P_2}$. The corresponding dissociation barriers for $\mathbf{P_1} \rightarrow \mathbf{P_{12}}$ and $\mathbf{P_2} \rightarrow \mathbf{P_{12}}$ are 26.1 and 31.1 kcal/mol, respectively. The secondary reactions including $\mathbf{P_1} \rightarrow \mathbf{P_3}$ ($HCN + {}^3HNO$), $\mathbf{P_1} \rightarrow \mathbf{P_4}$ ($HCNH + NO$), and $\mathbf{P_{12}} \rightarrow \mathbf{P_3}$ seem unlikely to occur considering the inter-H shift, since the two fragments of primary products should reorientate and must not separate.

3.2. Formation of Other Products. We also consider several other products $\mathbf{P_3}$ ($HCN + {}^3HNO$, −37.0), $\mathbf{P_4}$ ($HCNH + NO$, −21.1), $\mathbf{P_5}$ (${}^3H_2CO + N_2$, −67.3), $\mathbf{P_6}$ (${}^3HCOH + N_2$, −61.3), $\mathbf{P_7}$ (${}^3H_2NN + CO$, −54.9), $\mathbf{P_8}$ (${}^3HNNH + CO$, −49.7), $\mathbf{P_9}$ ($N_2H + HCO$, −43.3), $\mathbf{P_{10}}$ ($N_2H + HOC$, −1.8), and $\mathbf{P_{11}}$ ($H_2O + {}^3CN_2$, −29.7). The values in parentheses are relative energies with reference to the reactants **R**. Notice that $\mathbf{P_3}$, $\mathbf{P_5}$, $\mathbf{P_6}$, $\mathbf{P_7}$, $\mathbf{P_8}$, and $\mathbf{P_9}$ are lower in energy than the products $\mathbf{P_1}$ (−35.5) and $\mathbf{P_2}$ (−31.5).

As shown in Figure 4, $\mathbf{P_3}$ can only be obtained via the very high-energy transition states $\mathbf{TSa_2l_2}$ (39.9) or $\mathbf{TSk_4l_2}$ (46.9), while formation of $\mathbf{P_4}$ must proceed via $\mathbf{TSk_2m_2}$ (50.5). As shown in Figure 5, the lowest-energy product $\mathbf{P_5}$ can be formed either through the direct processes via $\mathbf{TSRP_5}$ (26.5) and $\mathbf{TSRP_5'}$ (46.9) or via the multistep processes $\mathbf{R} \rightarrow (\mathbf{a_1}, \mathbf{a_2}) \rightarrow \mathbf{b} \rightarrow (\mathbf{c_1}, \mathbf{c_2}) \rightarrow \mathbf{P_5}$ and $\mathbf{R} \rightarrow (\mathbf{a_1}, \mathbf{a_2}) \rightarrow \mathbf{n} \rightarrow (\mathbf{c_1}, \mathbf{c_2}) \rightarrow \mathbf{P_5}$, in which the respective highest-energy transition states are $\mathbf{TSa_1b}$ (32.3) and $\mathbf{TSa_2n}$ (59.3). The conversion from **a** to **c** via the four-membered ring intermediate **b** is associated with the successive ring-closure and ring-opening process, while that via the branched-chain isomer **n** is associated with the successive 1,2-O shift process, which is kinetically much less favorable. Despite numerous attempts, we are not able to locate the direct 1,3-O shift transition state $\mathbf{TSa_1c_1}$ from $\mathbf{a_1}$ to $\mathbf{c_1}$. Optimization of $\mathbf{TSa_1c_1}$ usually leads to $\mathbf{TSa_1b}$ or $\mathbf{TSbc_1}$. Formation of the remaining products $\mathbf{P_6 - P_{11}}$ must proceed via the sequence $\mathbf{a_1}$, **b**, and **c** (in Figure 5). Clearly, the rate-determining step for these products involves $\mathbf{TSa_1b}$. Thus, due to the high-energy and complexity of the formation pathways of $\mathbf{P_3 - P_{11}}$, the competition of these products with $\mathbf{P_1}$ and $\mathbf{P_2}$ is almost negligible. The secondary products of $\mathbf{P_3 - P_{11}}$ are then not considered further.

TABLE 4: Rate Constants ($\mathbf{cm^3\ Mol^{-1}\ s^{-1}}$) of the $\mathbf{{}^3CH_2 + N_2O}$ (R) → $\mathbf{H_2CNNO}$ ($\mathbf{a_1}$) Reaction at the QCISD(T)/6-311G(d,p)//B3LYP/6-31G(d,p)+ZPE Level

T(K)	TST	CVT	CVT/SCT
200.00	1.61×10^{-27}	9.03×10^{-30}	1.46×10^{-28}
222.00	4.90×10^{-26}	4.28×10^{-28}	2.39×10^{-27}
240.00	5.10×10^{-25}	6.01×10^{-27}	2.13×10^{-26}
255.00	2.81×10^{-24}	4.11×10^{-26}	1.14×10^{-25}
275.00	2.07×10^{-23}	3.89×10^{-25}	8.64×10^{-25}
295.00	1.17×10^{-22}	2.73×10^{-24}	5.22×10^{-24}
298.00	1.49×10^{-22}	3.58×10^{-24}	6.72×10^{-24}
300.00	1.75×10^{-22}	4.28×10^{-24}	7.93×10^{-24}
350.00	5.18×10^{-21}	1.91×10^{-22}	2.88×10^{-22}
400.00	6.86×10^{-20}	3.42×10^{-21}	4.58×10^{-21}
450.00	5.28×10^{-19}	3.32×10^{-20}	4.12×10^{-20}
500.00	2.78×10^{-18}	2.09×10^{-19}	2.46×10^{-19}
600.00	3.54×10^{-17}	3.50×10^{-18}	3.84×10^{-18}
800.00	9.92×10^{-15}	1.36×10^{-16}	1.38×10^{-16}
1000.00	8.32×10^{-15}	1.37×10^{-15}	1.34×10^{-15}
1200.00	3.73×10^{-14}	6.94×10^{-15}	6.63×10^{-15}
1400.00	1.16×10^{-13}	2.34×10^{-14}	2.20×10^{-14}
1600.00	2.84×10^{-13}	6.08×10^{-14}	5.65×10^{-14}
1800.00	5.90×10^{-13}	1.32×10^{-13}	1.22×10^{-13}
2000.00	1.09×10^{-12}	2.50×10^{-13}	1.80×10^{-13}

3.3. Reaction Mechanism and Comparison with Experiments. From Section 3.1, we know that the most energetically feasible channels for the title reaction may be:

$$\text{Path P}_1\text{:}\qquad \mathbf{R} \rightarrow \mathbf{a}\ (\mathbf{a_1}, \mathbf{a_2}) \rightarrow \mathbf{P_1}\ (\mathbf{H_2CN + NO}) \rightarrow \mathbf{P_{12}}\ (\mathbf{HCN + NO + H})$$

$$\text{Path P}_2\text{:}\qquad \mathbf{R} \rightarrow \mathbf{a_1} \rightarrow \mathbf{k}(\mathbf{k_1} - \mathbf{k_8}) \rightarrow \mathbf{P_2}\ (\mathbf{HCN + {}^3HON}) \rightarrow \mathbf{P_{12}}\ (\mathbf{HCN + NO + H})$$

The secondary product $\mathbf{P_{12}}$ is also included. Note that **Path P$_2$** is much less competitive than **Path P$_1$**. Formation of the other products seems unlikely due to kinetic hindrances.

The initial step in **Path P$_1$** and **Path P$_2$** is a barrier-consumed end-N attack process with a considerable barrier of 14.8 kcal/mol at the QCISD(T)/6-311G(d,p)//B3LYP/6-31G(d,p)+ZPE level. By means of our calculated potential energy surface, we roughly estimate the theoretical rate constants of the initial step, i.e., (${}^3CH_2 + N_2O$) **R** → (H_2CNNO) $\mathbf{a_1}$. Table 4 lists the conventional (TST) and canonical variational transition state theory (CVT) rate constants as well as with a small curvature tunneling correction (CVT/SCT) in a wide temperature range from 200 to 2000 K at the QCISD(T)/6-311G(d,p)//B3LYP/6-31G(d,p)+ZPE level. We can easily find that for such an addition process, the rate constant at room temperature is very small as $k(295K) = 5.22 \times 10^{-24}$ cm^3 $molecule^{-1}$ s^{-1}. Only at 1400 K, the CVT/SCT rate constant gets considerably larger at 2.20×10^{-14} cm^3 $molecule^{-1}$ s^{-1}. Note that the $^1CH_2 + N_2O$ reaction was found to be very fast with the room-temperature rate constant as 6.3×10^{-11} cm^3 $molecule^{-1}$ s^{-1}.[9] Therefore, the reaction $^3CH_2 + N_2O$ is negligible below about 1000 K and may only be of significance at higher temperatures. The exclusive high-temperature product is predicted to be $\mathbf{P_{12}}$ (HCN + NO + H).

It is useful to compare with available experiments concerning the title reaction. In 1995, Darwin and Moore[11] detected no change in $^3CH_2$ decay rates upon addition of N_2O at 295 K, and thus, they roughly assigned an upper limit of $k(295K)$ as 1.9×10^{-14} cm^3 $molecule^{-1}$ s^{-1}. Surely, this is in good agreement with our calculations. Since the title reaction may be important in high-temperature processes, it is very desirable to perform experimental measurements on the high-temperature rate constants for the title reaction in future.

Recently, Su et al.[12] carried out a time-resolved Fourier transform infrared (TR-FTIR) spectroscopy study on the possible products of the $^3CH_2 + N_2O$ reaction. They explicitly identified three nascent vibrationally excited products HCN, NO, and CO. The existence of the N_2H radical was also suggested. However, their observation of CO surely contradicts to our calculations predicting HCN, NO, and H as the exclusive observable high-temperature fragments. On the other hand, the available energy in Su et al.'s experiment,[12] 5.0 kcal/mol, is considerably lower than our calculated entrance end-N attack barrier (14.8 kcal/mol). We perform further higher-level QCISD(T)/6-311G(3df,2p)//B3LYP/6-31G(d,p)+ZPE single-point energy calculations, and the barrier is slightly increased to 15.2 kcal/mol. In addition, it is worthwhile to consider that the triplet reaction may proceed via a singlet−triplet intersection point to form singlet *cis*-H_2CNNO ($^1a_2$ in ref 10), instead of overcoming the high barrier at $\mathbf{TSRa_1}$ (In the singlet reaction, $^1CH_2 + N_2O$ lies higher in energy than $^3CH_2 + N_2O$. Yet the *cis*-H_2CNNO is formed without barrier and with 50.8 kcal/mol energy grain). However, we cannot locate any intersystem crossing points along the triplet reaction pathway ($\mathbf{R} \rightarrow \mathbf{TSRa_1}$) using the B3LYP and MP2 methods with the 6-31G(d,p) basis set. Note that we have considered nearly all possible attack channels in our work. The IR emission signals in Su et al.'s experiment may originate from secondary chemistry (perhaps $CH_2 + CH_2 \rightarrow CH_3 + CH$, followed by $CH + N_2O$, or reaction of CH_2 with NO impurity in the N_2O samples). Therefore, further experiments of this reaction are still very desirable to identify the products (most preferably, the product branching ratios).

It should be pointed out that based on their experimental observation, Su et al.[12] also proposed a reaction mechanism, i.e., $^3CH_2$ attack on end-O, N−N π bonding, and N−O π bonding. In our calculations, the end-O attack transition state $\mathbf{TSRP_5}$ is 11.7 kcal/mol higher than our most favorable end-N attack $\mathbf{TSRa_1}$ (as shown in Figure 4 and Figure 5). We cannot locate the N−N and N−O π bonding attack transition states, search of which usually leads to either the end-N attack $\mathbf{TSRa_1}$ or the middle-N attack **TSRn**. In fact, the CNN three-membered ring species **o** itself is 15.6 kcal/mol higher than **R**. Overall, the most energetically accessible channel for the $^3CH_2 + N_2O$ reaction should be initiated from the end-N attack.

3.4. Comparison with the Potential Energy Surface of $^1CH_2 + N_2O$. Now let us turn to the comparison with the $^1CH_2 + N_2O$ reaction. Very recently, we calculated the singlet CH_2N_2O potential energy surface and determined its reaction mechanism.[10] For both the $^1CH_2$ and $^3CH_2$ reactions with N_2O, the most feasible pathways are initiated by an end-N attack to form the chainlike species H_2CNNO, followed by a direct N−N dissociation to produce H_2CN + NO. For $^1CH_2 + N_2O$, a competitive concerted 1,3-H shift and N−N cleavage to product HCN + HNO may also take place, while for $^3CH_2 + N_2O$, formation of $\mathbf{P_2}$ (HCN + ^{3}HON) via the 1,4-H shift process is much less competitive than that of $\mathbf{P_1}$ (H_2CN + NO). Noticeably, such an end-N attack step is barrierless for the $^1CH_2$ reaction, as is consistent with the measured high rate constant 6.3×10^{-11} cm^3 $molecule^{-1}$ s^{-1} at room temperature.[9] Yet, the initial end-N attack needs a considerable barrier (14.8 kcal/mol) for the $^3CH_2$ reaction, which makes this reaction to be only of importance at high temperatures. On the other hand, for the $^1CH_2 + N_2O$ reaction, H_2CNNO can isomerize to the CNNO four-membered ring species, followed by the bimolecular extrusion to give the very low-lying yet less competitive product $N_2 + H_2CO$. For the present $^3CH_2 + N_2O$ reaction, similar pathway leading to $\mathbf{P_5}$ (N_2 + ^3H_2CO) also exists. Yet the CNNO four-membered ring isomer **b** and the isomerization transition state $\mathbf{TSa_1b}$ are 20.1 and 32.3 kcal/mol higher than **R** (in Figure 5). Then, N_2 formation can be excluded for the $^3CH_2 + N_2O$ reaction. CO is a minor product for the $^1CH_2 + N_2O$ reaction, while it seems unlikely for the $^3CH_2 + N_2O$ reaction even at high temperatures.

4. Conclusions

A detailed triplet potential energy surface of the $^3CH_2 + N_2O$ reaction system is investigated at the B3LYP and QCISD(T) (single-point) levels. The most feasible reaction pathways proceed via the initial end-N attack to form *cis*-H_2CNNO ($\mathbf{a_1}$), followed by easy conversion to *trans*-H_2CNNO $\mathbf{a_2}$. Both $\mathbf{a_1}$ and $\mathbf{a_2}$ can undergo the direct N−N rupture to form the primary product $\mathbf{P_1}$ (H_2CN + NO). Much less competitively, $\mathbf{a_1}$ can undergo a 1,4-H shift leading to (HCNNOH) $\mathbf{k_1}$, followed by the direct N−N cleavage to product $\mathbf{P_2}$ (HCN + ^{3}HON) or interconversion between the isomers $\mathbf{k_1}$−$\mathbf{k_8}$ and subsequent dissociation to $\mathbf{P_2}$. Both $\mathbf{P_1}$ (H_2CN + NO) and $\mathbf{P_2}$ (HCN + ^{3}HON) can undergo secondary dissociation to form the final same product $\mathbf{P_{12}}$ (HCN + NO + H). Formation of the other products seems unlikely due to kinetic hindrances. Moreover, since the initial end-N attack needs a considerable barrier of 14.8 kcal/mol, the $^3CH_2 + N_2O$ reaction may only play a role in very high temperatures with the exclusive product $\mathbf{P_{12}}$ (HCN + NO + H). Our calculated rate constants are in good agreement with the roughly estimated upper limit by Darwin and Moore.[11] Yet our predicted product distributions are in contradiction with recent TR-FTIR spectroscopy studies by Su et al.[12] This suggests a great need for future laboratory investigations on the title reaction.

Acknowledgment. This work is supported by the National Natural Science Foundation of China (No. G29892168, 20073014, 20103003). We are very thankful for the referees' invaluable comments.

References and Notes

(1) Laufer, A. H. *Rev. Chem. Intermed.* **1981**, *4*, 225.
(2) Winter, N. W. *Chem. Phys. Lett.* **1975**, *33*, 300.
(3) Homann, K. H.; Schweinfurth, H. *Ber. Bunsen-Ges. Pyhs. Chem.* **1981**, *85*, 569.
(4) Homann, K. H.; Schweinfurth, H. *Ber. Bunsen-Ges. Pyhs. Chem.* **1983**, *87*. 609.
(5) Homann, K. H.; Wagner, H. Gg. *11th Symp. (Int.) Combust.* **1967**, 371.
(6) Wagner, H. G. *17th Symp. (Int.) Combust.* **1979**, 3.
(7) Haynes, B. S. *Combust. Flame* **1977**, *28*, 81, 113.

(8) Hayden, C. C.; Neumark, D. M.; Shobatake, K.; Sparks, R. M.; Lee, R. T. *J. Phys. Chem*. **1982**, *76*, 3607.

(9) Koch, M.; Temps, F.; Wagener, R.; Wagner, H. G. *Ber. Bunsen-Ges. Phys. Chem*. **1990**, *94*, 645.

(10) Liu, J.; Feng, J.; Ding, Y.; Ren, A.; Wang, S.; Sun, C.; Kong, F. *J. Phys. Chem. A* **2001**, *105*, 5885.

(11) Darwin, D. C.; Moore, C. B. *J. Phys. Chem.* **1995**, *99*, 13468.

(12) Su, H.; Yang, J.; Zhong, J.; Kong, F. *Chem. Phys. Lett*. **1999**, *303*, 526.

(13) G98W A.7 Frisch, M. J.; Trucks, G. W.; Schlegel, H. B.; Scuseria, G. E.; Robb, M. A.; Cheeseman, J. R.; Zakrzewski, V. G.; Montgomery, J. A., Jr.; Stratmann, R. E.; Burant, J. C.; Dapprich, S.; Millam, J. M.; Daniels, A. D.; Kudin, K. N.; Strain, M. C.; Farkas, O.; Tomasi, J.; Barone, V.; Cossi, M.; Cammi, R.; Mennucci, B.; Pomelli, C.; Adamo, C.; Clifford, S.; Ochterski, J.; Petersson, G. A.; Ayala, P. Y.; Cui, Q.; Morokuma, K.; Malick, D. K.; Rabuck, A. D.; Raghavachari, K.; Foresman, J. B.; Cioslowski, J.; Ortiz, J. V.; Stefanov, B. B.; Liu, G.; Liashenko, A.; Piskorz, P.; Komaromi, I.; Gomperts, R.; Martin, R. L.; Fox, D. J.; Keith, T.; Al-Laham, M. A.; Peng, C. Y.; Nanayakkara, A.; Gonzalez, C.; Challacombe, M.; Gill, P. M. W.; Johnson, B. G.; Chen, W.; Wong, M. W.; Andres, J. L.; Head-Gordon, M.; Replogle, E. S.; Pople, J. A. *Gaussian 98*, revision A.7; Gaussian, Inc.: Pittsburgh, PA, 1998.

(14) Chuang, Y.-Y.; Corchado, J. C.; Fast, P. L.; Villà, J.; Hu, W.-P.; Liu, Y.-P.; Lynch, G. C.; Nguyen, K. A.; Jackels, C. F.; Gu, Zhen M.; Gossi, I.; Coitino, E. L.; Clayton, S.; Melissas, V. S. *POLYRATE*, version 8.0; University of Minnesota: Twin Cities, MN, 1998.